





Review

Recent Strategies for Hydrogen Peroxide Production by Metal-Free Carbon Nitride Photocatalysts

André Torres-Pinto , Maria J. Sampaio, Cláudia G. Silva * , Joaquim L. Faria  and Adrián M. T. Silva 

Laboratory of Separation and Reaction Engineering-Laboratory of Catalysis and Materials (LSRE-LCM), Faculdade de Engenharia, Universidade do Porto, Rua Roberto Frias, 4200-465 Porto, Portugal; andretp@fe.up.pt (A.T.-P.); mjsampaio@fe.up.pt (M.J.S.); jlfaria@fe.up.pt (J.L.F.); adrian@fe.up.pt (A.M.T.S.)
* Correspondence: cgsilva@fe.up.pt; Tel.: +351-22-041-4874

Received: 23 October 2019; Accepted: 19 November 2019; Published: 26 November 2019



Abstract: Hydrogen peroxide (H_2O_2) is a chemical which has gained wide importance in several industrial and research fields. Its mass production is mostly performed by the anthraquinone (AQ) oxidation reaction, leading to high energy consumption and significant generation of wastes. Other methods of synthesis found in the literature include the direct synthesis from oxygen and hydrogen. However, this H_2O_2 production process is prone to explosion hazard or undesirable by-product generation. With the growing demand of H_2O_2 , the development of cleaner and economically viable processes has been under intense investigation. Heterogeneous photocatalysis for H_2O_2 production has appeared as a promising alternative since it requires only an optical semiconductor, water, oxygen, and ideally solar light irradiation. Moreover, employing a metal-free semiconductor minimizes possible toxicity consequences and reinforces the sustainability of the process. The most studied metal-free catalyst employed for H_2O_2 production is polymeric carbon nitride (CN). Several chemical and physical modifications over CN have been investigated together with the assessment of different sacrificial agents and light sources. This review shows the recent developments on CN materials design for enhancing the synthesis of H_2O_2 , along with the proposed mechanisms of H_2O_2 production. Finally, the direct in situ generation of H_2O_2 , when dealing with the photocatalytic synthesis of added-value organic compounds and water treatment, is discussed.

Keywords: hydrogen peroxide; photocatalysis; carbon nitride; metal-free; oxygen reduction

1. Introduction

H_2O_2 is considered an environmentally friendly, active, and safe chemical in a broad range of applications, acting as a powerful oxidizing agent. H_2O_2 has been reported in environmental remediation, textile whitening, paper bleaching, chemical synthesis, cleansing of electronic materials, processing of metals, energy storage, and electric energy generation in fuel cells [1–3].

H_2O_2 is frequently present in the textile industry, reacting with the colouring matter during the bleaching process [4,5]. In organosynthesis, H_2O_2 has the capability to accelerate oxidation reactions, being exploited for the production of many fine and bulk chemicals [6]. Another application for H_2O_2 is in the field of fuel cells as it is a promising alternative energy carrier [7–10], due to its high energy density and ease/safety of storage (contrasting with H_2 that presents some storage issues [11]). H_2O_2 can play a crucial role in the removal of pollutants from aqueous or gaseous effluents, being commonly combined with catalysts, ozone, or a light source. Wet peroxide oxidation (with and without catalysts), Fenton and photo-Fenton oxidations, and sono-, electro-, or photo-chemical reactions are some of the main processes where H_2O_2 is employed for water and wastewater treatment [12–19]. Particularly,

H₂O₂ is widely used in photocatalytic water treatment because the addition or even in situ generation of H₂O₂ has been established as a promoter of the degradation of pollutants [20–32].

In response to an increasing H₂O₂ demand, different production processes have been developed and are currently operating at industry and laboratory scale [1]. However, many of these technologies often involve security issues regarding H₂/O₂ gas mixture, the use of organic solvents, metal catalysts, and the generation of undesirable by-products and solvent wastes [3]. Thus, to reduce these disadvantages, numerous approaches have been studied and developed for the synthesis of H₂O₂. These methods include: (i) chemical, sonochemical, and electrochemical processes, (ii) catalytic, and (iii) photocatalytic (metal-based or -free) systems.

H₂O₂ is produced mainly by the anthraquinone (AQ) route, commonly known as Riedl-Pfleiderer process [2,33–35]. This process is based on redox reactions [2,36,37], carried out in the presence of a mixture of organic solvents, e.g., ester/hydrocarbon or octanol/methyl-naphthalene. An alkylanthraquinone reacts with hydrogen, in the presence of a noble metal catalyst (e.g., Pt or Pd), and the corresponding alkylanthraquinol. The latter is oxidized under oxygenated conditions (air or O₂), generating H₂O₂ and the former alkylanthraquinone. The quinol species can be further hydrogenated and oxygenated under the same conditions producing H₂O₂ and tetrahydroanthraquinone. Afterwards, H₂O₂ is recovered from the organic solution with water to obtain a 30% H₂O₂ solution, which is then distilled under reduced pressure to remove impurities and increase its concentration. The anthraquinone process avoids implementing a H₂/O₂ gas mixture, which is known to be explosive, with this process being economically viable for large-scale production operations. However, there are still high operating costs associated with the acquisition of the raw materials, replacement of the catalysts, and the high energy requirement during the production procedure [2]. Another interesting technology for H₂O₂ generation consists on the application of sonochemistry which, by dissociation of oxygen and water, leads to the formation of H₂O₂ [38–41]. However, limitations of ultrasounds for chemical synthesis include long exposure time that can induce H₂O₂ decay and the difficulty in reactor design and process scale-up [42,43].

To reduce energy costs, the design of efficient and inexpensive catalytic processes has become imperative for the generation of H₂O₂. The use of metallic catalysts, such as Pd- and Au-based catalysts or metal oxides (e.g., Al₂O₃ or TiO₂), has been thoroughly documented due to their high selectivity [44–56]. Although several catalytic technologies have been discussed in the literature, the focus of this review is on the application of heterogeneous photocatalysis for H₂O₂ production. Briefly, in heterogeneous photocatalysis, an optical semiconductor is irradiated by an appropriate light source for its activation, leading to the formation of photogenerated electron/hole pairs which, under certain conditions, have the ability to produce H₂O₂ [57]. Depending on the reaction medium, the electronic properties of specific optical semiconductors, and the wavelength and intensity of the radiation source, heterogeneous photocatalysis can be adjusted to different processes (e.g., degradation of aqueous contaminants and production of high-value chemicals, among others [58,59]). Furthermore, photocatalytic processes may be employed under ambient temperature and pressure conditions and can be activated by free and inexhaustible solar light, further reducing the energy costs in comparison with traditional thermally activated routes. In a careful look at the literature, it was possible to retrieve more than 11,000 scientific reports on the various approaches for H₂O₂ synthesis (source: Scopus database, October 2018). Although photocatalytic production of H₂O₂ can be considered a recent topic, in recent years, the number of publications has been increasing significantly, which indicates that this technology could be considered an interesting alternative to traditional routes.

Metal-metal oxide hybrid catalysts have also been widely studied as promising candidates in the context of photocatalytic production of H₂O₂, owing to their high chemical stability and low toxicity [60–63]. Among all the metal elements, Ru, Bi, Co, and Cd are the most commonly combined with optical semiconductors, such as TiO₂ (the standard photocatalyst) [36,64–71]. Despite their high efficiency for several photocatalytic applications, metal catalysts present viability problems and poor

sustainability due to their high cost, difficulty of extraction from their ores, and possibility of leaching, which can contaminate the reaction medium and lead to the generation of hazardous wastes [72–75].

In this way, the development and optimization of metal-free structures as heterogeneous photocatalysts has been attracting wide interest. In the scope of metal-free photocatalytic H₂O₂ generation, the most employed material is polymeric carbon nitride (g-C₃N₄, here denoted as CN). Polymeric CN generally shows a relatively narrow band gap enabling visible light absorption, yet fast recombination of the photogenerated electron/hole pairs generally occurs. A sustainable process for photocatalytic H₂O₂ synthesis, besides requiring a visible-light activated metal-free material, requires the use of water instead of organic solvents (e.g., alcohols as sacrificial agents). CN can catalyse water splitting and selectively produce H₂O₂ under visible light irradiation through oxygen reduction [76–78].

Depending of the CN precursor and preparation method, the band potentials of CN (typically –1.12 and 1.58 eV, for the valence and conduction levels, respectively) are thermodynamically suitable for several applications, especially organic synthesis, H₂ production, and pollutants degradation [79–83]. Several reports have shown that pristine CN materials hold a small specific surface area and low chemisorption of oxygen, commonly leading to low photocatalytic efficiencies [79,84]. Thus, several modification strategies have been pursued to increase the efficiency of CN-based photocatalysts, such as soft templating approaches, exfoliation, elemental doping, or heterojunction formation [79,85]. However, some authors report that, besides material engineering, photochemical considerations are a rather important issue to discuss since proper charge separation and transfer kinetics are needed for efficient H₂O₂ production [86,87].

Recently, Haider et al. [88] briefly summarized some studies concerning the synthesis of hybrid CN-based photocatalysts for H₂O₂ production. Regardless of the several studies reported on the use of CN for H₂O₂ production by heterogeneous photocatalysis, a consolidated knowledge focused on the influence of both metal-free CN structure and the manipulation of the operating conditions for improving H₂O₂ productivity is still missing.

In the present review, the photocatalytic production of H₂O₂ using metal-free CN is explored. Herein, the influence of the catalyst tuning and process optimization is correlated and discussed. The capability of simultaneously producing H₂O₂ during the synthesis of value-added organic compounds and their ability to induce high photocatalytic degradation of organic pollutants present in waters is a crucial point taken into consideration in this study.

2. H₂O₂ Production by Carbon Nitride Photocatalysts

The photocatalytic production of H₂O₂ can occur through several pathways, which may differ depending on the use of metallic or non-metallic catalysts. The use of metal-based photocatalysts to generate H₂O₂ is well discussed in the literature [62,63,89–93]. However, using non-metals, such as CN materials, the reaction pathway for H₂O₂ generation is still under study. A general scheme is depicted in Figure 1, illustrating the main steps occurring after photoactivation of CN in the presence of molecular oxygen and water. After light absorption, the migration of electrons from the valence band (VB) to the conduction band (CB) occurs. Then, electrons (e[−]) in the CB and photogenerated holes (h⁺) migrate to the surface of the photocatalyst and participate in reduction and oxidation reactions, respectively.

To improve H₂O₂ synthesis with photoactive CN, it is necessary to understand the reactions that take place at the photocatalyst surface. The pathway for H₂O₂ synthesis using CN photocatalysts is generally ascribed to the capacity of this material to drive two-electron oxygen reduction. Figure 2 represents the photoactivation of CN with visible light and the mechanism for H₂O₂ production suggested by Shiraishi et al. [94]. The authors propose that the electron/hole pairs are localized in the 1, 4 and 2, 6 positions highlighted in Figure 2, with the negatively charged sites attracting oxygen and later reacting with the trapped protons in nearby N atoms. Then, a selected alcohol is used as sacrificial agent. Photoexcited electrons react with O₂, leading to the formation of the 1,4-endoperoxide species, which results in the liberation of H₂O₂. At the same time, a proton donor (e.g., an alcohol or

water) undergoes oxidation and yields protons that contribute to generating H_2O_2 [76]. The efficient formation of the endoperoxide species suppresses one- and four-electron reduction of O_2 (Equation (1), (2), respectively), improving the selectivity of two-electron reduction of O_2 (Equation (3)). However, O_2 on pristine CN preferably undergoes reduction to $\text{O}_2^{\bullet-}$ via one-electron reduction (Equation (1)), while on modified CN materials with more surface defects, a more facile production of H_2O_2 is achieved (Equation (3)) [95].

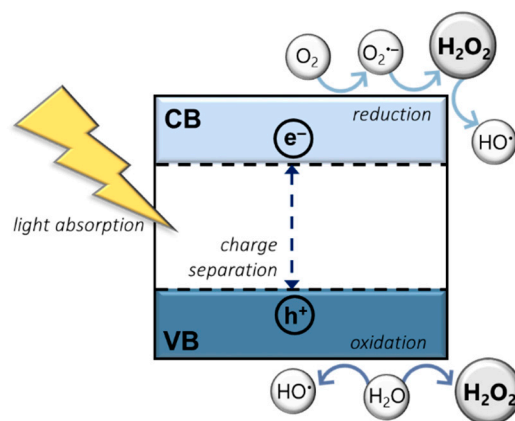


Figure 1. Photocatalytic activation and formation of reactive oxygen species in the presence of oxygen (O_2) and water (H_2O). H_2O_2 = hydrogen peroxide; $\text{O}_2^{\bullet-}$ = superoxide radical; HO^\bullet = hydroxyl radical; VB = valence band; CB = conduction band; e^- = electrons; h^+ = photogenerated holes.

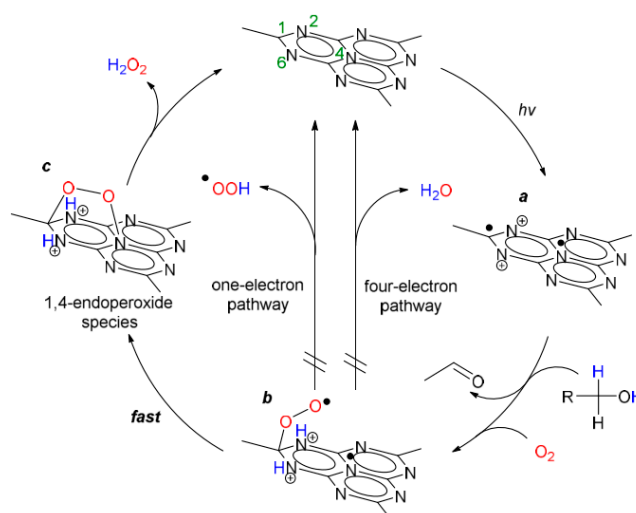
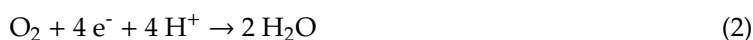


Figure 2. Proposed mechanism for selective formation of H_2O_2 on the photoactivated CN surface. Reprinted with permission from reference [94]. Copyright 2015 American Chemical Society.

Shiraishi et al. [76] reported Raman spectroscopy and electron spin resonance (ESR) studies that in their work, rationalizing the mechanism behind the selective two-electron reduction of O_2 on photoexcited CN. After irradiation, the Raman spectrum of CN catalyst in an O_2 -saturated solution showed a new broad peak at 891 cm^{-1} , ascribed to bond vibrations in the 1,4-endoperoxide species.

Concerning the ESR analyses, products of one-electron reduction of O₂ were not found, proving that O₂ is being selectively reduced to H₂O₂ [76].

In another work, authors reported the formation of H₂O₂ by a two-step single-electron reduction of O₂ (Equations (1) and (4)), via the reduction of O₂^{•-} (reduction product of O₂) to H₂O₂ [96]. Additionally, under suitable conditions (i.e., with an appropriate VB energy), water oxidation may occur, generating H₂O₂ (Equation (5)) [96,97]. H₂O₂ can also evolve via the transformation of HO[•] formed from the hole-oxidation of HO⁻ (Equation (6), (7)) [96]. These pathways enable the production of H₂O₂ by both oxidation and reduction routes (Figure 1). However, H₂O₂ production from water and O₂ is hard to facilitate using the bulk CN photocatalyst, owing to the small thermodynamic driving force between the VB energy (1.4 V) and the water oxidation potential (0.8 V) [76,98–100].



H₂O₂ can drive the production of HO[•] in the presence of light (Equation (8)), depending on the radiation wavelength and catalyst employed [20,22,23]. The degradation of H₂O₂ to form HO[•] radicals has a potential of +0.39 V [101] and, therefore, is favourable to occur on the CB of the semiconductor. In this way, the presence of H₂O₂ and photoactivated CN can generate HO[•] radicals. These radicals are desired for several applications in environmental remediation, such as in water treatment, e.g., abatement of phenols [102], dyes [103], and antibiotics [104].

3. Enhancing Photocatalytic Activity of Carbon Nitride

In the following sections, metal-free strategies to modify CN will be overviewed and discussed to understand their influence on the efficiency and productivity of H₂O₂ photosynthesis. Several approaches can be found in the literature for improving the efficiency of this material, including thermal treatments, chemical substitutions with other carbon materials, or with specific organic molecules [105–107]. All these approaches are summarized in the following sections along with the correspondent experimental conditions of the photocatalytic tests and their ensuing results. The H₂O₂ productivity is depicted in terms of the highest amount produced after a respective irradiation time and moles of H₂O₂ per catalyst load and time, i.e., production rate (μmol g_{cat}⁻¹ h⁻¹).

Multiple articles have reported the preparation of CN using distinct precursors and their posterior application using different experimental conditions [76,107,108]. In Table 1, the results in terms of H₂O₂ production using several neat CN materials are listed. Metal-free CN materials modified by several approaches are also shown in this table and discussed below.

Shiraishi et al. [76] reported the application of a metal-free CN material for H₂O₂ production using various alcohols for improving H₂O₂ selectivity. In this study, high H₂O₂ selectivity (>90%) was achieved by using aqueous solutions of aliphatic or aromatic alcohols, namely ethanol, propan-2-ol, butan-2-ol, and benzyl alcohol. Concerning the proton donor, benzyl alcohol and propan-2-ol yielded the higher amounts of H₂O₂. Then, testing the system using solar irradiation with or without a light filter (λ > 420 nm), higher selectivity for H₂O₂ formation is obtained when CN is activated by visible light rather than using the total spectrum range. This is due to ultraviolet light leading to the unwanted decomposition of H₂O₂.

Comparing the same matrix, light source, and gas but changing the precursor used in the catalyst synthesis, a much higher rate is achieved when using melamine [107] instead of cyanamide precursor [76].

The same group investigated the use of silica templates for changing the textural properties of CN [94]. The increase of surface defects leads to the formation of a large number of primary amines, which act as active sites for four-electron reduction of O_2 . A decrease on the selectivity towards H_2O_2 formation was observed in this system with the highest production rate of $188 \mu\text{mol g}_{\text{cat}}^{-1} \text{h}^{-1}$ and 60% selectivity.

3.1. Surface Chemistry Modulation

Li et al. [105] reported that H_2O_2 production can be improved up to 14 times in the absence of an organic electron scavenger in the presence of carbon-vacancies (Cv). This study revealed that a post-treatment with argon led to the destruction of the crystallinity of CN and, therefore, produce defects, i.e., carbon vacancies (Figure 3). The Cv enhanced the trapping of the photogenerated electrons. Moreover, amino groups were formed and promoted electron transfer and changed the H_2O_2 production pathway from two-electron direct reduction of O_2 to sequential one-electron reduction of O_2 (Figure 3). In addition, it was also found that Cv decreased the band gap energy but did not interfere with the CB potential. This study showed that the chemisorption of O_2 on the catalyst was enhanced with this modification. The effect of nitrogen vacancies (Nv) was also assessed, with the H_2O_2 production being much lower than using materials with Cv. The highest H_2O_2 production rate obtained for CN-Cv and CN-Nv was 900 and $150 \mu\text{mol g}_{\text{cat}}^{-1} \text{h}^{-1}$, respectively, under visible light ($\lambda > 420 \text{ nm}$) irradiation.

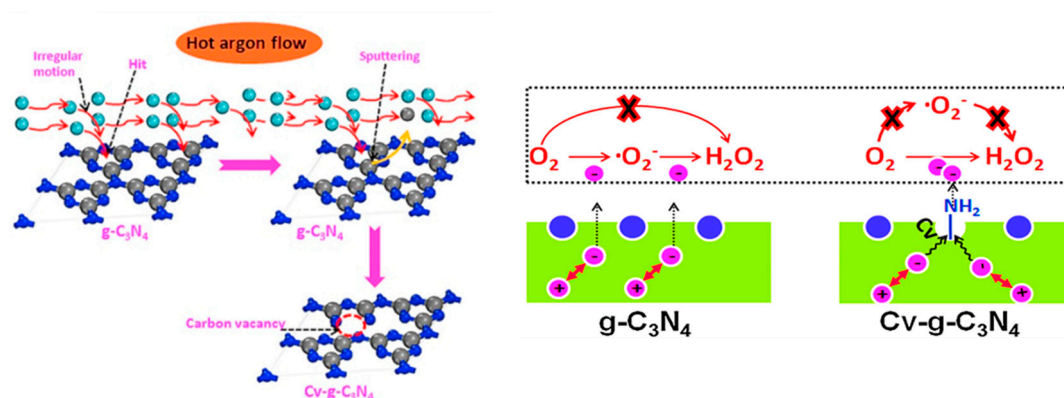


Figure 3. Formation of carbon vacancy on CN (left) and H_2O_2 formation pathway (right). Adapted with permission from reference [105]. Copyright 2016 Elsevier B.V.

In another study, the effect of the presence of nitrogen defects on a CN catalyst has been discussed in terms of their ability for reducing electron-hole recombination and improving the contact between the reactant and active sites on the catalyst surface [109].

Thermal post-treatment of bulk CN drives the cleavage between tri-*s*-triazine moieties forming nitride vacancies and increasing $C\equiv N$ groups on the matrix (Figure 4) [110]. This is accomplished by the incorporation of electron-deficient or π -conjugated monomers that falls for low bands energy potentials and inhibit the recombination. Moreover, the incorporation of strong electron acceptor groups can reduce the band gap energy and positively shift both CB and VB. The same authors investigated the impact of the saturated gas by testing the catalyst activity in the presence of O_2 , air, and N_2 at the same conditions. It was observed that the H_2O_2 production rate was enhanced by saturating the suspensions with these gases, following the order $O_2 > \text{air} > N_2$. These results seems to indicate that most H_2O_2 production derives from O_2 reduction with a small contribution from water oxidation.

Finally, another approach was performed by a plasma treatment with a power input of high voltage under H_2 atmosphere with the main aim of the inclusion of N vacancies on the CN matrix [111]. These vacancies act as active sites for O_2 adsorption and also have the capability to promote electron transfer, thus accelerating the reduction step. Furthermore, this catalyst suppressed the decomposition

of H_2O_2 , which resulted in a very high production rate of $2167 \mu\text{mol g}_{\text{cat}}^{-1} \text{h}^{-1}$ in the presence of ethanol and pure O_2 .

3.2. Functionalization

The most recent studies found in the scope of metal-free photocatalytic H_2O_2 production consisted on the combination of CN with carbon, via doping or bonding with carbon nanotubes (CNT). Using C-doped CN, a positive shift of the band potentials was found (Figure 5). This change on the VB accelerates water oxidation, and on the CB enhances oxygen reduction, improving H_2O_2 production owing to reduced kinetic barriers of the corresponding reactions. It was verified that H_2O_2 production is strongly dependent on the carbon content and the electronic structure of CN. The synthesized material with highest H_2O_2 production simultaneously presented the highest formation and lowest decomposition rate constants, yielding a maximum H_2O_2 rate of $365 \mu\text{mol g}_{\text{cat}}^{-1} \text{h}^{-1}$ in a 5% propan-2-ol solution with O_2 saturation [112]. This study strengthened the claim of the formation and decomposition of H_2O_2 being two competitive reactions, with the formation following a zero-order kinetics due to continuous O_2 saturation, and the decomposition following a first-order kinetics.

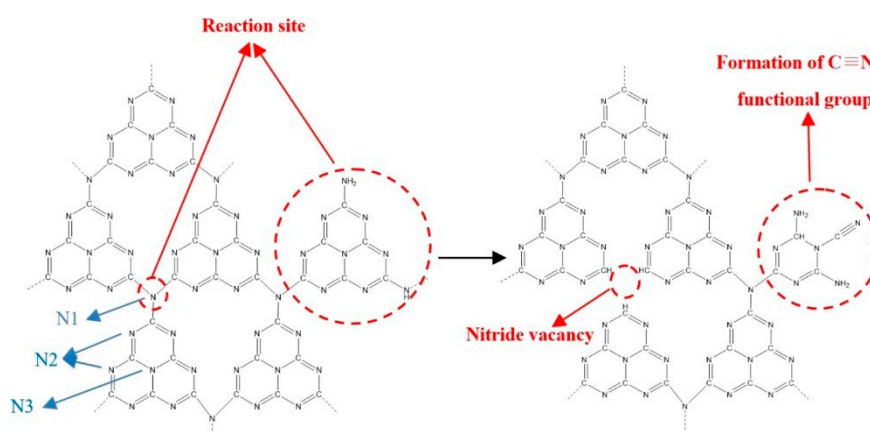


Figure 4. Nitrogen defects on CN matrix after thermal treatment. Adapted with permission from reference [110]. Copyright 2018 Elsevier B.V.

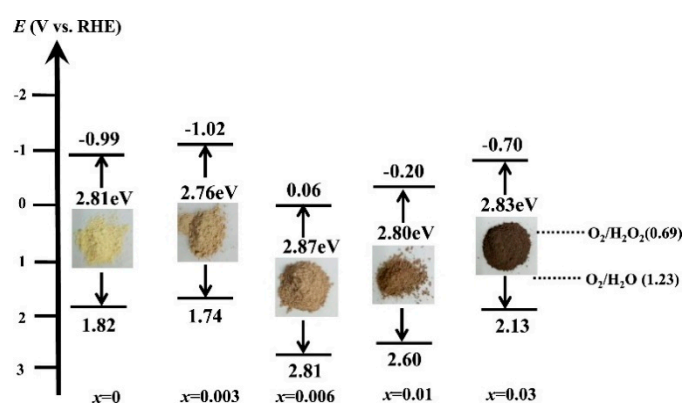


Figure 5. Energy levels of carbon (C)-doped CN (x denotes de carbon doping load). Reprinted with permission from reference [112]. Copyright 2018 Science Press and Dalian Institute of Chemical Physics, Chinese Academy of Sciences.

The covalent combination between CNT and CN (CN-CNT) promotes the sequential two-step pathway (Figure 2), using formic acid or methanol as electron donors. However, CN-CNT catalyses both water oxidation and O_2 reduction, forming H_2O_2 without the need of an electron donor. This

was proved by the presence of benzoquinone, which depresses H_2O_2 production by inhibiting the sequential two-step O_2 reduction. This material reached a maximum production rate of $487 \mu\text{mol g}_{\text{cat}}^{-1} \text{h}^{-1}$ using a 5:95 formic acid:water solution in O_2 -saturated conditions [106].

Another strategy to improve the CN photocatalytic activity is the anchoring of organic compounds, such as AQ. Moon et al. [113] showed that H_2O_2 production was dependent on the concentration of AQ and that, for higher AQ loads, there is a light block effect. When AQ is physisorbed on CN, the H_2O_2 production is improved. The authors explained the results based on the reutilization studies in which it was found that AQ remain at the CN surface, thus achieving a highly stable photocatalyst. H_2O_2 production was enhanced not only due to the higher H_2O_2 formation but also as a consequence of lower H_2O_2 decomposition. The authors also tested several AQ sources which lead to the functionalization with different groups. The material with COOH groups showed the highest formation and lowest decomposition rates, enabling continuous production over extended irradiation time in the presence of an electron donor. Furthermore, the apparent quantum yield profile resembles its absorption spectrum, meaning that efficient optical absorption and charge collection are achieved; however, with some useless recombination remains.

Benzene doping was tested by Kim et al. [114], achieving an H_2O_2 production rate of $300 \mu\text{mol g}_{\text{cat}}^{-1} \text{h}^{-1}$ that was obtained in O_2 -saturated conditions and using a 10% ethanol aqueous solution. The increase of photoactivity compared to the bulk material was mainly ascribed to the structure distortion (Figure 6), which was promoted by the substitution of the N atoms in the matrix by benzene with a much higher molecule size. In addition, the presence of benzene leads to an easier charge transfer and hinders the recombination of electron/hole pairs.

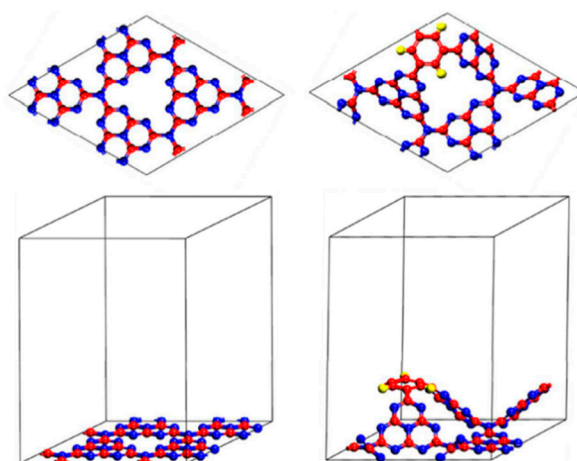


Figure 6. Top and side view of CN matrix before (left) and after distortion by benzene doping (right). Red, blue, and yellow represent carbon, nitrogen, and hydrogen atoms, respectively. Adapted with permission from reference [114]. Copyright 2017 American Chemical Society.

Several authors have reported doping CN with nitrogen, oxygen and phosphate as an efficient technique for increasing the efficiency for H_2O_2 production [115–117]. In the case of N-doping, it was described that it decreases O_2 adsorption energy and enhances charge transfer [115]. Doping with oxygen promoted higher light absorption and efficient charge separation with a lower recombination rate [116]. The anchoring of phosphate on CN led to enhanced O_2 adsorption, which was ascribed as the main reason for the increased H_2O_2 productivity [117].

3.3. Construction of Heterostructures

The combination of carbon materials, like fullerene (C_{60}), graphene oxide (GO), and reduced graphene oxide (rGO), with CN have shown to promote a negative impact for H_2O_2 production owing to the higher affinity to one-electron O_2 reduction route [108]. Even with O_2 saturation and in the

presence of a propan-2-ol solution (regarded as one of the best proton donors for this process [76]), the yield of H_2O_2 achieved with these hybrid materials was relatively low.

Aromatic diimides are n-type semiconductors with high electron mobility and stability. Therefore, their incorporation on the CN structure can lead to a positive shift on both VB and CB bands, owing to the high electron affinity [107].

Reports have been shown that pyromellitic diimide (PDI) units increase the rates of H_2O_2 formation as the valence band shifts promoting water oxidation to O_2 , facilitating H_2O_2 production (Figure 7). Shiraishi et al. [107] reported the use of a CN-PDI material using water and propan-2-ol as solvents. With this study, the authors obtained a much higher rate ($573 \mu\text{mol g}_{\text{cat}}^{-1} \text{h}^{-1}$) for H_2O_2 production when the alcohol was present, due its capacity of acting as a strong proton donor [107]. In another work, the CN material was modified with biphenyl diimide (BDI) [77], and the effect of polymerization temperature was evaluated. The authors found an optimal temperature of 653 K, which yielded $6.8 \mu\text{mol}$ of H_2O_2 after 24 h of irradiation corresponding to a rate of $5.7 \mu\text{mol g}_{\text{cat}}^{-1} \text{h}^{-1}$. By increasing the polymerization temperature, the authors found a significant catalyst weight loss, followed by a decrease on the photocatalytic activity of the resulting materials. Moreover, the amount of BDI on the CN was studied, and among all the resulting materials, the best photocatalytic activity was achieved with a molar ratio of 50% BDI in the catalyst, yielding $41 \mu\text{mol}$ after 48 h of irradiation and a $9.7 \mu\text{mol g}_{\text{cat}}^{-1} \text{h}^{-1}$ rate. According to the calculated apparent quantum yield, BDI doping is more effective than PDI. BDI doping leads to a positive shift on the VB and CB, enabling water oxidation and promoting H_2O_2 formation (Figure 7). Additionally, ab initio calculations suggest that there is a significant spatial charge separation (h^+ in BDI and e^- on melem; on PDI both h^+ and e^- are on melem) which hinders their recombination improving H_2O_2 formation.

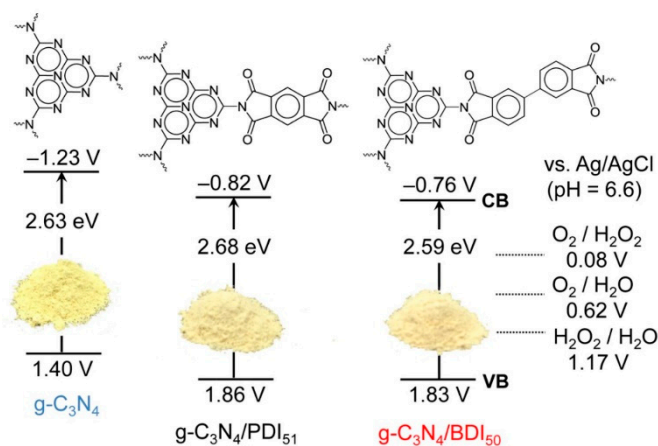


Figure 7. Electronic structure of different catalysts. Reprinted with permission from reference [77]. Copyright 2016 American Chemical Society. PDI = pyromellitic diimide; BDI = biphenyl diimide.

The photoactivity of catalysts, such as CN, which are π -conjugated semiconductors, depends on the density and mobility of the photoformed charge carriers [118]. The same authors that used PDI also reported the combination of CN with mellitic triimide (MTI) [78]. The incorporation of MTI units and the subsequent stacking of melem layers can lead to efficient inter and intralayer charge transfer. Therefore, the CN-MTI catalyst showed improvements on the conductivity and charge transport, as well as a higher photoactivity, compared with the pristine CN towards H_2O_2 production.

PDI-, BDI-, and MTI-modified CN has also been combined with reduced graphene oxide (rGO). In general, rGO has the ability to trap photogenerated electrons from the CB of the CN-PDI material, acting as active sites for the two-electron reduction of O_2 . On the other hand, CN-PDI-rGO photocatalyst promoted slight decomposition of H_2O_2 . However, using a physical mixture of CN-PDI and rGO, no significant effect was observed, which can be ascribed to the low interaction between CN-PDI and rGO materials [119].

Structures of CN coupled with boron nitride (BN) were prepared to further enhance electron transfer [120,121]. The composite made with BN quantum dots favours the acceleration of charge transfer and the decrease of recombination [120]. The material with BN nanosheets resulted in an elevated production ($1400 \mu\text{mol g}_{\text{cat}}^{-1} \text{h}^{-1}$) since the authors managed to decrease H_2O_2 decomposition while maintaining very high formation rates [121]. The addition of BN seems to promote the separation of holes hindering recombination. Kofuji et al. have explored the combination of a CN-PDI material with BN [122]. The photogenerated holes in the VB on the CN/PDI moiety move to the VB of BN leading to their entrapment, which enhances charge separation and promotes H_2O_2 production. Moreover, addition of rGO further inhibits the recombination of electrons and holes. The material consisting of CN-PDI combined with both BN and rGO resulted in the highest H_2O_2 production rates due to promoting both water oxidation and oxygen reduction (Figure 8), while increasing the charge transfer. Moreover, these studies also supported the impact of the presence of an alcohol as proton donor. The use of propan-2-ol as solvent increased the H_2O_2 production rate by a factor of 50, comparing with water.

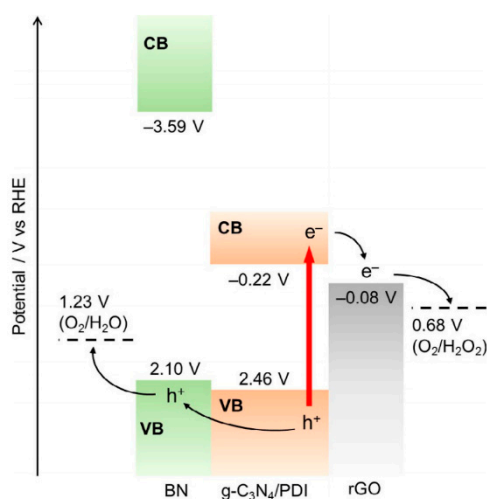


Figure 8. Energy diagram of the CN-PDI-reduced graphene oxide (rGO)- boron nitride (BN) catalyst. Reprinted with permission from reference [122]. Copyright 2018 Wiley-VCH Verlag GmbH & Co. KGaA, Weinheim, Germany.

Wang et al. [96] investigated the use of perylene imide (PI), to create a Z-scheme heterojunction with CN nanosheets for enhancing the oxidative power of photogenerated holes [123]. The CN-PI structures led to higher H_2O_2 production; however, for excessive PI amounts, light absorption by the nanosheets was compromised. PI seems to favour the separation of charge carriers and leads to faster interfacial charge transfer (Figure 9). The addition of PI changes the production of H_2O_2 from a direct two-electron oxygen reduction to a two-channel pathway (Equations (3) and (4)). Moreover, the presence of PI inhibits the subsequent decomposition of H_2O_2 [96].

Table 1. Metal-free CN-based materials, experimental conditions, and respective photocatalytic results.

Modification on CN	Preparation Method	Experimental Conditions	Photocatalytic Results		Ref.
			H ₂ O ₂ Generated (μmol)	Production Rate ($\mu\text{mol g}_{\text{cat}}^{-1} \text{h}^{-1}$)	
None	Thermal polymerization of cyanamide under N ₂ atmosphere	9/1 (v/v) propan-2-ol/water (5 mL); 4 g L ⁻¹ ; 2000 W Xe lamp ($\lambda > 420 \text{ nm}$); O ₂	60 μmol (24 h)	125	[76]
None	Thermal polymerization of cyanamide under N ₂ atmosphere	9/1 (v/v) benzyl alcohol/water matrix (5 mL); 4 g L ⁻¹ ; 2000 W Xe lamp ($\lambda > 420 \text{ nm}$); O ₂	109 μmol (24 h)	227	[76]
None	Thermal polymerization of cyanamide under N ₂ atmosphere	9/1 (v/v) ethanol/water (5 mL); 4 g L ⁻¹ ; 2000 W Xe lamp ($\lambda > 420 \text{ nm}$); O ₂	30 μmol (24 h)	63	[76]
None	Thermal polymerization of cyanamide under N ₂ atmosphere	9/1 (v/v) butan-1-ol/water (5 mL); 4 g L ⁻¹ ; 2000 W Xe lamp ($\lambda > 420 \text{ nm}$); O ₂	18 μmol (24 h)	38	[76]
None	Thermal polymerization of cyanamide under N ₂ atmosphere	9/1 (v/v) propan-1-ol/water (5 mL); 4 g L ⁻¹ ; 2000 W Xe lamp ($\lambda > 420 \text{ nm}$); O ₂	6.3 μmol (24 h)	13	[76]
None	Thermal polymerization of cyanamide under N ₂ atmosphere	9/1 (v/v) propan-2-ol/water (5 mL); 4 g L ⁻¹ ; sunlight; O ₂	120 μmol (9 h)	667	[76]
None	Thermal polymerization of cyanamide under N ₂ atmosphere	9/1 (v/v) propan-2-ol/water (5 mL); 4 g L ⁻¹ ; sunlight ($\lambda > 420 \text{ nm}$); O ₂	70 μmol (9 h)	389	[76]
None	Thermal polymerization of melamine	9/1 (v/v) propan-2-ol/water (30 mL); 1.7 g L ⁻¹ ; 2000 W Xe lamp ($\lambda > 420 \text{ nm}$); O ₂	148 μmol (6 h)	493	[107]
Adding surface defects	Silica-templated thermal polymerization of cyanamide under N ₂ atmosphere	9/1 (v/v) ethanol/water (5 mL); 4 g L ⁻¹ ; 2000 W Xe lamp ($\lambda > 420 \text{ nm}$); O ₂	90 μmol (24 h)	188	[94]
Adding C vacancies	Thermal polymerization of melamine and further treatment under Ar atmosphere	water (100 mL); 1.0 g L ⁻¹ ; 300 W Xe lamp ($\lambda > 420 \text{ nm}$); O ₂	9 μmol (1 h)	90	[105]
Adding N vacancies	Thermal polymerization of melamine and further treatment under H ₂ atmosphere	water (100 mL); 1.0 g L ⁻¹ ; 300 W Xe lamp ($\lambda > 420 \text{ nm}$); O ₂	1.5 μmol (1 h)	15	[105]
Adding N vacancies	Thermal polymerization of dicyandiamide and photo-assisted post-treatment with hydrazine	20% (v) propan-2-ol/water (60 mL); 0.83 g L ⁻¹ ; solar simulator ($\lambda > 420 \text{ nm}$); O ₂	12.1 μmol (2.5 h)	97	[109]
Adding N vacancies	Thermal polymerization of melamine and further calcinated with sodium borohydride	water (100 mL); 1.0 g L ⁻¹ ; 300 W Xe lamp ($\lambda \geq 420 \text{ nm}$); O ₂	30.0 μmol (1 h)	300	[110]
Adding N vacancies	Thermal polymerization of melamine and further calcinated with sodium borohydride	water (100 mL); 1.0 g L ⁻¹ ; 300 W Xe lamp ($\lambda \geq 400 \text{ nm}$); air	17.0 μmol (1 h)	170	[110]
Adding N vacancies	Thermal polymerization of melamine and further calcinated with sodium borohydride	water (100 mL); 1.0 g L ⁻¹ ; 300 W Xe lamp ($\lambda \geq 400 \text{ nm}$); N ₂	2.5 μmol (1 h)	25	[110]
Adding N vacancies	Thermal polymerization of melamine and H ₂ plasma treatment	50% (v) ethanol/water (200 mL); 1.0 g L ⁻¹ ; 250 W high-pressure sodium lamp ($\lambda > 400 \text{ nm}$); O ₂	26000 μmol (12 h)	2167	[111]
C doping	Thermal polymerization of melamine and sonication with glucose	5/95 (v/v) propan-2-ol/water; 1.0 g L ⁻¹ ; 300 W Xe lamp; O ₂	38.1 μmol (4 h)	318	[112]

Table 1. Cont.

Modification on CN	Preparation Method	Experimental Conditions	Photocatalytic Results		Ref.
			H ₂ O ₂ Generated (μmol)	Production Rate ($\mu\text{mol g}_{\text{cat}}^{-1} \text{h}^{-1}$)	
Carbon nanotubes combination	Thermal polymerization of dicyandiamide and ammonium chloride and mixed with carbon nanotubes	5/95 (v/v) formic acid/water (100 mL); 1.0 g L ⁻¹ ; 300 W Xe lamp ($\lambda \geq 400$ nm); O ₂	48.7 μmol (1 h)	487	[106]
Carbon nanotubes combination	Thermal polymerization of dicyandiamide and ammonium chloride and mixed with carbon nanotubes	5/95 (v/v) methanol/water (100 mL); 1.0 g L ⁻¹ ; 300 W Xe lamp ($\lambda \geq 400$ nm); O ₂	23.1 μmol (1 h)	231	[106]
Carbon nanotubes combination	Thermal polymerization of dicyandiamide and ammonium chloride and mixed with carbon nanotubes	water (100 mL); 1.0 g L ⁻¹ ; 300 W Xe lamp ($\lambda \geq 400$ nm); O ₂	1.3 μmol (1 h)	13	[106]
AQ-COOH coupling	Thermal polymerization of melamine and sonication with anthraquinone (AQ)-2-carboxylic acid	1/9 (v/v) propan-2-ol/water; 0.5 g L ⁻¹ ; 150 W Xe lamp ($\lambda > 400$ nm); O ₂	no data	361	[108]
AQ-COOH coupling	Thermal polymerization of melamine and sonication with anthraquinone-2-carboxylic acid	1/9 (v/v) propan-2-ol/water; 0.5 g L ⁻¹ ; 150 W Xe lamp ($\lambda > 400$ nm); air	no data	270	[108]
AQ-NH ₂ coupling	Thermal polymerization of melamine and sonication with 2-aminoanthraquinone	1/9 (v/v) propan-2-ol/water; 0.5 g L ⁻¹ ; 150 W Xe lamp ($\lambda > 400$ nm); O ₂	no data	233	[108]
AQ-SO ₃ ⁻ coupling	Thermal polymerization of melamine and sonication with sodium anthraquinone-2-sulfonate	1/9 (v/v) propan-2-ol/water; 0.5 g L ⁻¹ ; 150 W Xe lamp ($\lambda > 400$ nm); O ₂	no data	131	[108]
AQ-OH coupling	Thermal polymerization of melamine and sonication with 2-hydroxymethylanthraquinone	1/9 (v/v) propan-2-ol/water; 0.5 g L ⁻¹ ; 150 W Xe lamp ($\lambda > 400$ nm); O ₂	no data	86.9	[108]
AQ-COOH coupling	Thermal polymerization of melamine and sonication with anthraquinone-2-carboxylic acid	water; 0.5 g L ⁻¹ ; 150 W Xe lamp ($\lambda > 400$ nm); O ₂	no data	24	[108]
Benzene substitution	Thermal polymerization of urea with trimesic acid	1/9 (v/v) ethanol/water (30 mL); 0.5 g L ⁻¹ ; 300 W Xe lamp ($\lambda > 420$ nm); O ₂	275 μmol (3 h)	300	[114]
N doping	Thermal polymerization of melamine, sonication with tetracycline hydrochloride and further thermal exfoliation	3/7 (v/v) propan-2-ol/water (100 mL); 0.5 g L ⁻¹ ; solar simulator ($\lambda > 420$ nm); O ₂	14 μmol (1 h)	279	[115]
O doping	Thermal polymerization of dicyandiamide with nitric acid and hydrothermal post-treatment	water (50 mL); 1.0 g L ⁻¹ ; 250 W high-pressure sodium lamp ($\lambda > 400$ nm); O ₂	760 μmol (6 h)	633	[116]
Phosphate doping	Thermal polymerization of melamine and hydrothermal treatment with H ₃ PO ₄	2.6 mM EDTA aqueous solution (200 mL); 1.0 g L ⁻¹ ; 250 W high-pressure sodium lamp ($\lambda > 400$ nm); O ₂	1080 μmol (6 h)	900	[117]
CN-C ₆₀	Thermal polymerization of melamine and C ₆₀	1/9 (v/v) propan-2-ol/water; 0.5 g L ⁻¹ ; 150 W Xe lamp ($\lambda > 400$ nm); O ₂	no data	63.2	[108]
CN-GO	Thermal polymerization of melamine and sonication with GO	1/9 (v/v) propan-2-ol/water; 0.5 g L ⁻¹ ; 150 W Xe lamp ($\lambda > 400$ nm); O ₂	no data	62.3	[108]
CN-rGO	Thermal polymerization of melamine and sonication with hydrazine-reduced GO	1/9 (v/v) propan-2-ol/water; 0.5 g L ⁻¹ ; 150 W Xe lamp ($\lambda > 400$ nm); O ₂	no data	74.3	[108]

Table 1. Cont.

Modification on CN	Preparation Method	Experimental Conditions	Photocatalytic Results		Ref.
			H ₂ O ₂ Generated (μmol)	Production Rate (μmol g _{cat} ⁻¹ h ⁻¹)	
CN-PDI	Thermal polymerization of melamine and pyromellitic dianhydride (PMDA)	water (30 mL); 1.7 g L ⁻¹ ; 2000 W Xe lamp (λ > 420 nm); O ₂	50.6 μmol (48 h)	21	[107]
CN-PDI	Thermal polymerization of melamine and pyromellitic dianhydride (PMDA)	9/1 (v/v) propan-2-ol/water (30 mL); 1.7 g L ⁻¹ ; 2000 W Xe lamp (λ > 420 nm); O ₂	210 μmol (6 h)	700	[107]
CN-BDI	Thermal polymerization of melamine and biphenyl tetracarboxylic dianhydride (BTCDA)	9/1 (v/v) propan-2-ol/water (30 mL); 3.3 g L ⁻¹ ; solar simulator (λ > 400-500 nm); O ₂	22.2 μmol (2 h)	111	[77]
CN-BDI	Thermal polymerization of melamine and biphenyl tetracarboxylic dianhydride (BTCDA)	water (30 mL); 1.7 g L ⁻¹ ; solar simulator (λ > 420 nm); O ₂	11.6 μmol (24 h)	10	[77]
CN-MTI	Thermal polymerization of melem and mellitic acid trianhydride (MTA)	water (30 mL); 1.7 g L ⁻¹ ; Xe lamp (λ > 420 nm); O ₂	27.5 μmol (24 h)	23	[78]
CN-PDI-rGO	Hydrothermal treatment of melem and GO and thermal polymerization with PMDA	water (30 mL); 1.7 g L ⁻¹ ; 2000 W Xe lamp (λ > 420 nm); O ₂	60 μmol (48 h)	25	[119]
CN-PDI-rGO	Hydrothermal treatment of melem and GO and thermal polymerization with PMDA	9/1 (v/v) propan-2-ol/water (30 mL); 1.7 g L ⁻¹ ; 2000 W Xe lamp (λ > 420 nm); O ₂	550 μmol (9 h)	1222	[119]
CN-PDI-BN	Sonication of melem and CN and thermal polymerization with PMDA	water (30 mL); 1.7 g L ⁻¹ ; 200 W Xe lamp (λ > 420 nm); O ₂	28 μmol (24 h)	23	[122]
CN-PDI-BN	Sonication of melem and CN and thermal polymerization with PMDA	9/1 (v/v) propan-2-ol/water (30 mL); 1.7 g L ⁻¹ ; 200 W Xe lamp (λ > 420 nm); O ₂	370 μmol (6 h)	1233	[122]
CN-PDI-rGO-BN	Sonication of melem, GO and CN and thermal polymerization with PMDA	water (30 mL); 1.7 g L ⁻¹ ; 200 W Xe lamp (λ > 420 nm); O ₂	37 μmol (24 h)	31	[122]
CN-PDI-rGO-BN	Sonication of melem, GO and CN and thermal polymerization with PMDA	9/1 (v/v) propan-2-ol/water (30 mL); 1.7 g L ⁻¹ ; 200 W Xe lamp (λ > 420 nm); O ₂	550 μmol (6 h)	1833	[122]
CN-PI	Thermal polymerization of melamine and cyanuric acid and reflux condensation reaction with perylene tetracarboxylic dianhydride (PTCDA) and imidazole	water (30 mL); 1.7 g L ⁻¹ ; 300 W Xe lamp (λ > 420 nm); no data	120 μmol (2 h)	1200	[96]
CN-BP	Thermal polymerization of urea followed by sonication with N-methyl-2-pyrrolidone and BP	1/9 (v/v) propan-2-ol/water (30 mL); 1.7 g L ⁻¹ ; 300 W Xe lamp (λ > 420 nm); O ₂	540 μmol (1 h)	540	[124]
CN-BN	Hydrothermal treatment and thermal polymerization of thiourea and melamine and sonication with BN dots	1/9 (v/v) propan-2-ol/water (50 mL); 1.0 g L ⁻¹ ; 300 W Xe lamp (λ > 420 nm); O ₂	72.3 μmol (1 h)	72.3	[120]
CN-BN	Thermal polymerization of urea and BN nanosheets	1/9 (v/v) methanol/water (40 mL); 0.5 g L ⁻¹ ; 300 W Xe lamp (λ > 305 nm); O ₂	112 μmol (4 h)	1400	[121]

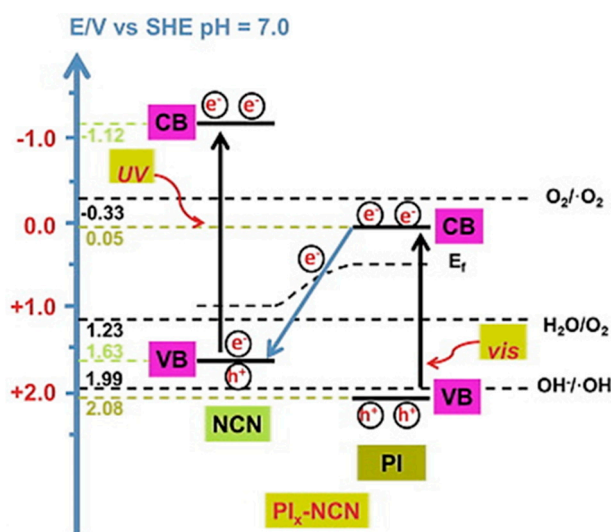


Figure 9. Energy diagram for the Z-scheme structure of the CN-perylene imide (PI) photocatalyst. Adapted with permission from reference [96]. Copyright 2017 Elsevier B.V.

The combination of CN and black phosphorus (BP) was reported by Zheng et al. [124]. This composite allowed for a higher H_2O_2 productivity than the lone CN, owing to BP being highly reactive to oxygen.

To compare the different structures and experimental conditions by an unbiased parameter, the apparent quantum yield (AQY) and the solar-to-chemical conversion (SCC) of H_2O_2 production are typically applied. These coefficients were calculated by the respective authors and were collected in Table 2. The AQY gives the information about the formation of H_2O_2 relative to the number of incident photons and relates the stoichiometric amount of H_2O_2 formed with a specific light intensity and emission wavelength [125]. The SCC is related to the performance of a catalyst to yield H_2O_2 , relating the free energy of H_2O_2 formation and the total incident energy [125]. Therefore, higher AQY and SCC values can demonstrate the photoactivity efficiency and proneness to selectively generate H_2O_2 . For instance, Kofuji et al. [122] reported the hybrid CN-PDI-BN-rGO, which yielded the highest reported values of AQY and SCC compared to other works, as well as the highest rates for H_2O_2 production.

Table 2. Solar-to-chemical conversion (SCC) and apparent quantum yield (AQY) efficiencies for some studies. Nv = nitrogen vacancies.

Material	AQY/%	SCC/%	Ref.
CN-PDI	2.6	0.10	[77]
CN-PI	3.2	no data	[96]
CN-Nv	4.3	0.26	[110]
CN-BDI	4.6	0.13	[77]
CN-PDI-BN	4.8	0.19	[122]
CN-MTI	6.0	0.18	[78]
CN-PDI-rGO	6.1	0.20	[119]
CN-PDI-BN-rGO	7.3	0.27	[122]

4. Photocatalytic Application with In Situ H_2O_2 Generation

H_2O_2 is used in numerous applications and, due to its oxidizing power, is commonly added in many systems, namely in the abatement of organic contaminants and in fine chemistry, to improve conversion and accelerate the reaction. For instance, the application of sonochemistry has been reported for the simultaneous in situ generation of H_2O_2 and degradation of organics [39,40]. The coupling of ultrasounds and photocatalysts (sonophotocatalysis) has been employed for the degradation of

phenol and 4-chlorophenol with titania-based materials, where the presence of in situ evolved H_2O_2 markedly improved the degradation process [126]. Particularly, in photocatalysis, the presence of H_2O_2 is reported to increase the mineralization or removal rates of several organics [12–19] and enhance the selectivity of photochemical synthesis [6]. Therefore, the in situ generation of H_2O_2 in applications in which it is used as reactant is not only an advantage in terms of process design but also in terms of cost reduction, as described in the next sections.

4.1. Pollutant Degradation

The photodegradation of organic molecules and removal of biological contaminants using metal-free CN materials has been extensively investigated. Some works report the addition of H_2O_2 , resulting in the enhancement of the degradation process [22,127–131]. In most cases, the CN photocatalyst acts as a Fenton-mimic since it turns H_2O_2 into HO^\bullet which attack the pollutants, leading to increased mineralization [20,132,133]. This interesting duality of CN is worth of being explored, and several authors have already verified the in situ evolution of H_2O_2 to enhance the oxidative abatement of contaminants. As previously discussed, metal-free CN, under visible-light, leads to the formation of H_2O_2 , and is used for the removal of several organic compounds by photocatalysis. Many studies report the formation of H_2O_2 simultaneously to the degradation of the contaminant molecules [20,23,120,134–141]. The degradation is accompanied by the formation of reactive oxygen species (ROS), H_2O_2 being detected during the photocatalytic experiments. Two studies recently followed the time-dependent H_2O_2 concentration along the photocatalytic degradation reaction of phenol [95,142]. Zhang et al. detected H_2O_2 using CN nanosheets under visible light irradiation with the production being markedly dependent in the structure of CN, yielding larger amounts for more exfoliated materials which promote selective two-electron O_2 reduction [95]. Additionally, the formation of highly reactive oxygen species promoted phenol degradation, such as HO^\bullet originated from H_2O_2 decomposition. The presence of O_2 in an aqueous solution can lead to the formation of H_2O_2 and other reactive oxygen species which aid the oxidation of organic molecules. H_2O_2 is a fast reacting molecule; however, its stabilization and production is very dependent of the medium [1]. For instance, the pH dependency of H_2O_2 is known and, in more acidic media, H_2O_2 is more stable than in an alkaline environment [143]. However, CN has been proven to act efficiently in all pH range since this material presents amphoteric properties [144,145]. Relative to H_2O_2 formation, it is observed that many other factors have to be taken into consideration, namely the content in dissolved oxygen, pollutant initial concentration, catalyst load and light source. The work developed by Svoboda et al. [142] somewhat showed the impact of these parameters on H_2O_2 production since quenching experiments lead to changes on the degradation of phenol (sacrificial agent for H_2O_2 formation). However, the use of scavenging species, to study H_2O_2 formation and decomposition, may suffer interference owing to their degradation by different reactive oxy-species. This can hinder or facilitate the generation of H_2O_2 leading to ambiguous results. Svoboda et al. [142] investigated the degradation of phenol using CN nanosheets obtained from the thermal post-treatment of melamine-derived bulk CN. This allowed for an increase of the surface area of the material, leading to much higher photoactivity. In this work, an impressive H_2O_2 production rate of $3300 \mu\text{mol g}_{\text{cat}}^{-1} \text{h}^{-1}$ was reported, using visible-LEDs with a maximum emission wavelength of $\lambda = 416 \text{ nm}$, continuous air purging and a phenol initial concentration of 20 mg L^{-1} .

Furthermore, using differently-substituted phenolic compounds and exfoliated CN it is possible to obtain high production rates between 633 and $3103 \mu\text{mol g}_{\text{cat}}^{-1} \text{h}^{-1}$ [146], using visible-light emitting diodes and continuous air saturation. This study contemplates the relation between O_2 concentration and H_2O_2 production, establishing that as the dissolved oxygen content increases up to 21% there is an increase in H_2O_2 formation. Moreover, the exfoliated CN in this work was tested in a propan-2-ol aqueous solution, achieving a H_2O_2 production rate of $19,200 \mu\text{mol g}_{\text{cat}}^{-1} \text{h}^{-1}$.

To date, the combination of oxidation driven by in situ evolved H_2O_2 in CN photocatalysts with other AOPs for water treatment has been reported for ozonation and persulfate activation [147,148].

These two studies investigate the in situ evolution of H₂O₂ during the reaction and discuss the synergic effect that promoted the removal of the contaminant molecules. However, it is interesting to point out that H₂O₂ is fundamental in the Fenton reaction. In addition, in a homogeneous Fenton system, the treated water matrix remains with dissolved iron which has to be separated. Iron-doped CN photocatalysts result on the combination of traditional Fenton and CN photocatalysis which enhances oxidation by promoting a two-channel pathway of H₂O₂ reduction to generate HO•. In this way, many authors have synthesized iron-doped CN to try combat the disadvantage of dissolved iron in the mineralized waters [149–152].

CN has been applied as metal-free photocatalyst for the degradation of several organic pollutants, but the generation of H₂O₂ was not monitored in the publications [153,154]; thus, they are not considered in this review.

4.2. Fine Chemistry

In the case of selective organic synthesis, there are reports of H₂O₂ addition while employing metal-free CN photocatalysts [155,156]. The presence of H₂O₂ improves the oxidation of selected molecules, such as the conversion of toluene to benzaldehyde [155] or of cyclic olefins to the respective epoxides [156]. However, there have been reports where H₂O₂ formation was observed in the presence of both visible light and a CN catalyst. Lopes et al. [157] achieved very high production rates of ca. 5000 μmol g_{cat}⁻¹ h⁻¹ using nanosheets of CN in an anisyl alcohol solution. In that work, H₂O₂ was formed as a by-product of the oxidation of aromatic alcohols into the corresponding aldehydes. The simultaneous formation of H₂O₂ is a further advantage to the selective organic synthesis owing to the oxidizing power of H₂O₂, such as Zhang et al. [158] describes with an oxygen-enriched CN material employed for the transformation of amines into imines.

5. Conclusions and Future Prospects

This review article summarizes the state-of-the-art on modified metal-free carbon nitride photocatalysts for the selective evolution of H₂O₂, a high-value and multi-faceted chemical. Conventional processes for H₂O₂ synthesis are generally characterized by high energy consumption and waste generation. The latest studies, employing sustainable metal-free carbon nitride materials and clean aqueous matrices as solvents, show an emergent photocatalytic technology for H₂O₂ generation, including the smart tailoring of these materials for optimal conversion. Moreover, the ambivalence of the photocatalytic process, with simultaneous production and direct application of H₂O₂, has already been explored for pollutant degradation and fine chemical synthesis. The referred studies provide a favourable starting point to achieve sustainability in the industry of H₂O₂ production, albeit more research has to be performed to develop the necessary scale up operation, productivity enhancement, and overall process optimization.

Author Contributions: Conceptualization, all authors; methodology, A.T.-P. and M.J.S.; investigation, A.T.-P.; resources, J.L.F.; C.G.S. and A.M.T.S.; writing—original draft preparation, A.T.-P. and M.J.S.; writing—review and editing, all authors; supervision, C.G.S.; J.L.F. and A.M.T.S.

Funding: This work was financially supported by project NORTE-01-0145-FEDER-031049 (InSpeCt, PTDC/EAM-AMB/31049/2017) funded by the European Regional Development Fund (ERDF) through NORTE 2020 - Programa Operacional Regional do NORTE and by national funds (PIDDAC) through FCT-Fundação para a Ciência e a Tecnologia, and by projects POCI-01-0145-FEDER-030674, POCI-01-0145-FEDER-031398 and POCI-01-0145-FEDER-029600, funded by ERDF through COMPETE2020 – Programa Operacional Competitividade e Internacionalização (POCI) – and by national funds through FCT. We would also like to thank the scientific collaboration under project “AIProcMat@N2020 - Advanced Industrial Processes and Materials for a Sustainable Northern Region of Portugal 2020”, with the reference NORTE-01-0145-FEDER-000006, supported by NORTE 2020 under the Portugal 2020 Partnership Agreement through ERDF, and project Associate Laboratory LSRE-LCM - UID/EQU/50020/2019 funded by national funds through FCT/MCTES (PIDDAC). C.G.S. acknowledges the FCT Investigator Programme (IF/00514/2014) with financing from the European Social Fund (ESF) and the Human Potential Operational Programme.

Conflicts of Interest: The authors declare no conflict of interest.

References

1. Hess, W.T. Hydrogen Peroxide. In *Kirk-Othmer Encyclopedia of Chemical Technology*, 5th ed.; John Wiley & Sons, Inc.: Hoboken, NJ, USA, 2007; Volume 14, pp. 35–79.
2. Samanta, C. Direct synthesis of hydrogen peroxide from hydrogen and oxygen: An overview of recent developments in the process. *Appl. Catal. A Gen.* **2008**, *350*, 133–149. [[CrossRef](#)]
3. Campos-Martin, J.M.; Blanco-Brieva, G.; Fierro, J.L.G. Hydrogen Peroxide Synthesis: An Outlook beyond the Anthraquinone Process. *Angew. Chem. Int. Ed.* **2006**, *45*, 6962–6984. [[CrossRef](#)]
4. Asghar, A.; Raman, A.A.A.; Wan Daud, W.M.A. Advanced oxidation processes for in-situ production of hydrogen peroxide/hydroxyl radical for textile wastewater treatment: A review. *J. Clean. Prod.* **2015**, *87*, 826–838. [[CrossRef](#)]
5. Karmakar, S.R. Chapter 6—Bleaching of textiles. In *Chemical Technology in the Pre-Treatment Processes of Textiles*; Elsevier: Amsterdam, The Netherlands, 1999; Volume 12, pp. 160–216.
6. Sato, K.; Aoki, M.; Noyori, R. A “Green” Route to Adipic Acid: Direct Oxidation of Cyclohexenes with 30 Percent Hydrogen Peroxide. *Science* **1998**, *281*, 1646–1647. [[CrossRef](#)]
7. Yamazaki, S.-I.; Siroma, Z.; Senoh, H.; Ioroi, T.; Fujiwara, N.; Yasuda, K. A fuel cell with selective electrocatalysts using hydrogen peroxide as both an electron acceptor and a fuel. *J. Power Sour.* **2008**, *178*, 20–25. [[CrossRef](#)]
8. Shaegh, S.A.M.; Nguyen, N.-T.; Ehteshami, S.M.M.; Chan, S.H. A membraneless hydrogen peroxide fuel cell using Prussian Blue as cathode material. *Energy Environ. Sci.* **2012**, *5*, 8225–8228. [[CrossRef](#)]
9. Yamada, Y.; Yoneda, M.; Fukuzumi, S. A Robust One-Compartment Fuel Cell with a Polynuclear Cyanide Complex as a Cathode for Utilizing H₂O₂ as a Sustainable Fuel at Ambient Conditions. *Chem. Eur. J.* **2013**, *19*, 11733–11741. [[CrossRef](#)] [[PubMed](#)]
10. Yang, F.; Cheng, K.; Wu, T.; Zhang, Y.; Yin, J.; Wang, G.; Cao, D. Preparation of Au nanodendrites supported on carbon fiber cloth and its catalytic performance to H₂O₂ electroreduction and electrooxidation. *RSC Adv.* **2013**, *3*, 5483–5490. [[CrossRef](#)]
11. Fukuzumi, S. Bioinspired Energy Conversion Systems for Hydrogen Production and Storage. *Eur. J. Inorg. Chem.* **2008**, *2008*, 1351–1362. [[CrossRef](#)]
12. Perathoner, S.; Centi, G. Wet hydrogen peroxide catalytic oxidation (WHPCO) of organic waste in agro-food and industrial streams. *Top. Catal.* **2005**, *33*, 207–224. [[CrossRef](#)]
13. Rokhina, E.V.; Virkutyte, J. Environmental Application of Catalytic Processes: Heterogeneous Liquid Phase Oxidation of Phenol With Hydrogen Peroxide. *Crit. Rev. Environ. Sci. Technol.* **2010**, *41*, 125–167. [[CrossRef](#)]
14. Debellefontaine, H.; Chakchouk, M.; Foussard, J.N.; Tissot, D.; Striolo, P. Treatment of organic aqueous wastes: Wet air oxidation and wet peroxide oxidation®. *Environ. Pollut.* **1996**, *92*, 155–164. [[CrossRef](#)]
15. Domingues, F.S.; Freitas, T.K.F.D.S.; de Almeida, C.A.; de Souza, R.P.; Ambrosio, E.; Palácio, S.M.; Garcia, J.C. Hydrogen peroxide-assisted photocatalytic degradation of textile wastewater using titanium dioxide and zinc oxide. *Environ. Technol.* **2017**, *40*, 1223–1232. [[CrossRef](#)] [[PubMed](#)]
16. Gomes, H.T.; Miranda, S.M.; Sampaio, M.J.; Silva, A.M.T.; Faria, J.L. Activated carbons treated with sulphuric acid: Catalysts for catalytic wet peroxide oxidation. *Catal. Today* **2010**, *151*, 153–158. [[CrossRef](#)]
17. Ribeiro, R.S.; Silva, A.M.T.; Figueiredo, J.L.; Faria, J.L.; Gomes, H.T. Removal of 2-nitrophenol by catalytic wet peroxide oxidation using carbon materials with different morphological and chemical properties. *Appl. Catal. B Environ.* **2013**, *140*, 356–362. [[CrossRef](#)]
18. Ribeiro, R.S.; Silva, A.M.T.; Figueiredo, J.L.; Faria, J.L.; Gomes, H.T. Catalytic wet peroxide oxidation: A route towards the application of hybrid magnetic carbon nanocomposites for the degradation of organic pollutants. A review. *Appl. Catal. B Environ.* **2016**, *187*, 428–460. [[CrossRef](#)]
19. Ribeiro, R.S.; Silva, A.M.T.; Pastrana-Martínez, L.M.; Figueiredo, J.L.; Faria, J.L.; Gomes, H.T. Graphene-based materials for the catalytic wet peroxide oxidation of highly concentrated 4-nitrophenol solutions. *Catal. Today* **2015**, *249*, 204–212. [[CrossRef](#)]
20. Cui, Y.; Huang, J.; Fu, X.; Wang, X. Metal-free photocatalytic degradation of 4-chlorophenol in water by mesoporous carbon nitride semiconductors. *Catal. Sci. Technol.* **2012**, *2*, 1396–1402. [[CrossRef](#)]
21. Yao, Y.; Wu, G.; Lu, F.; Wang, S.; Hu, Y.; Zhang, J.; Huang, W.; Wei, F. Enhanced photo-Fenton-like process over Z-scheme CoFe₂O₄/g-C₃N₄ Heterostructures under natural indoor light. *Environ. Sci. Pollut. Res.* **2016**, *23*, 21833–21845. [[CrossRef](#)]

22. Kumar, A.; Kumar, A.; Sharma, G.; Naushad, M.; Veses, R.C.; Ghfar, A.A.; Stadler, F.J.; Khan, M.R. Solar-driven photodegradation of 17- β -estradiol and ciprofloxacin from waste water and CO₂ conversion using sustainable coal-char/polymeric-g-C₃N₄/rGO metal-free nano-hybrids. *New. J. Chem.* **2017**, *41*, 10208–10224. [[CrossRef](#)]
23. Zhou, C.; Lai, C.; Huang, D.; Zeng, G.; Zhang, C.; Cheng, M.; Hu, L.; Wan, J.; Xiong, W.; Wen, M.; et al. Highly porous carbon nitride by supramolecular preassembly of monomers for photocatalytic removal of sulfamethazine under visible light driven. *Appl. Catal. B Environ.* **2018**, *220*, 202–210. [[CrossRef](#)]
24. Su, M.; He, C.; Sharma, V.K.; Asi, M.A.; Xia, D.; Li, X.Z.; Deng, H.; Xiong, Y. Mesoporous zinc ferrite: Synthesis, characterization, and photocatalytic activity with H₂O₂/visible light. *J. Hazard. Mater.* **2012**, *211*, 95–103. [[CrossRef](#)] [[PubMed](#)]
25. Jia, Y.; Lee, B.W.; Liu, C. Magnetic ZnFe₂O₄ Nanocubes: Synthesis and Photocatalytic Activity with Visible Light/H₂O₂. *IEEE Trans. Magn.* **2017**, *53*, 1–5. [[CrossRef](#)]
26. Xu, J.; Wang, H.; Gu, H.; Zeng, C.; Yang, Y. Facile synthesis of Cu₂O nanocubes and their enhanced photocatalytic property assisted by H₂O₂. *Asian J. Chem.* **2013**, *25*, 1733–1736.
27. Kalam, A.; Al-Sehemi, A.G.; Assiri, M.; Du, G.; Ahmad, T.; Ahmad, I.; Pannipara, M. Modified solvothermal synthesis of cobalt ferrite (CoFe₂O₄) magnetic nanoparticles photocatalysts for degradation of methylene blue with H₂O₂/visible light. *Results Phys.* **2018**, *8*, 1046–1053. [[CrossRef](#)]
28. Deng, X.; Wang, C.; Shao, M.; Xu, X.; Huang, J. Low-temperature solution synthesis of CuO/Cu₂O nanostructures for enhanced photocatalytic activity with added H₂O₂: Synergistic effect and mechanism insight. *RSC Adv.* **2017**, *7*, 4329–4338. [[CrossRef](#)]
29. Pesakhov, S.; Benisty, R.; Sikron, N.; Cohen, Z.; Gomelsky, P.; Khozin-Goldberg, I.; Dagan, R.; Porat, N. Effect of hydrogen peroxide production and the Fenton reaction on membrane composition of *Streptococcus pneumoniae*. *BBA Biomembr.* **2007**, *1768*, 590–597. [[CrossRef](#)]
30. Pham, A.N.; Xing, G.; Miller, C.J.; Waite, T.D. Fenton-like copper redox chemistry revisited: Hydrogen peroxide and superoxide mediation of copper-catalyzed oxidant production. *J. Catal.* **2013**, *301*, 54–64. [[CrossRef](#)]
31. Fujihira, M.; Satoh, Y.; Osa, T. Heterogeneous photocatalytic oxidation of aromatic compounds on TiO₂. *Nature* **1981**, *293*, 206. [[CrossRef](#)]
32. Chiou, C.-H.; Wu, C.-Y.; Juang, R.-S. Influence of operating parameters on photocatalytic degradation of phenol in UV/TiO₂ process. *Chem. Eng. J.* **2008**, *139*, 322–329. [[CrossRef](#)]
33. Nishimi, T.; Kamachi, T.; Kato, K.; Kato, T.; Yoshizawa, K. Mechanistic Study on the Production of Hydrogen Peroxide in the Anthraquinone Process. *Eur. J. Org. Chem.* **2011**, *2011*, 4113–4120. [[CrossRef](#)]
34. Hans-Joachim, P.G.R. Production of Hydrogen Peroxide. US Patent 2158525, 10 October 1935.
35. Thenard, L.J. Observations sur des nouvelles combinaisons entre l'oxygène et divers acides. *Ann. Chim. Phys.* **1818**, *8*, 306–312.
36. Kato, S.; Jung, J.; Suenobu, T.; Fukuzumi, S. Production of hydrogen peroxide as a sustainable solar fuel from water and dioxygen. *Energy Environ. Sci.* **2013**, *6*, 3756–3764. [[CrossRef](#)]
37. Sandelin, F.; Oinas, P.; Salmi, T.; Paloniemi, J.; Haario, H. Kinetics of the Recovery of Active Anthraquinones. *Ind. Eng. Chem. Res.* **2006**, *45*, 986–992. [[CrossRef](#)]
38. Lim, M.; Son, Y.; Khim, J. The effects of hydrogen peroxide on the sonochemical degradation of phenol and bisphenol A. *Ultrason. Sonochem.* **2014**, *21*, 1976–1981. [[CrossRef](#)] [[PubMed](#)]
39. Pétrier, C. 31—The use of power ultrasound for water treatment. In *Power Ultrasonics*; Gallego-Juárez, J.A., Graff, K.F., Eds.; Woodhead Publishing: Oxford, UK, 2015; pp. 939–972.
40. Shende, T.; Andaluri, G.; Suri, R.P.S. Kinetic model for sonolytic degradation of non-volatile surfactants: Perfluoroalkyl substances. *Ultrason. Sonochem.* **2019**, *51*, 359–368. [[CrossRef](#)] [[PubMed](#)]
41. Ziembowicz, S.; Kida, M.; Koszelnik, P. The impact of selected parameters on the formation of hydrogen peroxide by sonochemical process. *Sep. Purif. Technol.* **2018**, *204*, 149–153. [[CrossRef](#)]
42. Kiss, A.A.; Geertman, R.; Wierschem, M.; Skiborowski, M.; Gielen, B.; Jordens, J.; John, J.J.; Van Gerven, T. Ultrasound-assisted emerging technologies for chemical processes. *J. Chem. Technol. Biotechnol.* **2018**, *93*, 1219–1227. [[CrossRef](#)]
43. Ashokkumar, M. Advantages, Disadvantages and Challenges of Ultrasonic Technology. In *Ultrasonic Synthesis of Functional Materials*; Springer International Publishing: Cham, Switzerland, 2016; pp. 41–42.
44. Chinta, S.; Lunsford, J.H. A mechanistic study of H₂O₂ and H₂O formation from H₂ and O₂ catalyzed by palladium in an aqueous medium. *J. Catal.* **2004**, *225*, 249–255. [[CrossRef](#)]

45. Dissanayake, D.P.; Lunsford, J.H. Evidence for the Role of Colloidal Palladium in the Catalytic Formation of H_2O_2 from H_2 and O_2 . *J. Catal.* **2002**, *206*, 173–176. [[CrossRef](#)]
46. Dissanayake, D.P.; Lunsford, J.H. The direct formation of H_2O_2 from H_2 and O_2 over colloidal palladium. *J. Catal.* **2003**, *214*, 113–120. [[CrossRef](#)]
47. Liu, Q.; Lunsford, J.H. The roles of chloride ions in the direct formation of H_2O_2 from H_2 and O_2 over a Pd/SiO₂ catalyst in a H₂SO₄/ethanol system. *J. Catal.* **2006**, *239*, 237–243. [[CrossRef](#)]
48. Lunsford, J.H. The direct formation of H_2O_2 from H_2 and O_2 over palladium catalysts. *J. Catal.* **2003**, *216*, 455–460. [[CrossRef](#)]
49. Choudhary, V.R.; Gaikwad, A.G.; Sansare, S.D. Activation of Supported Pd Metal Catalysts for Selective Oxidation of Hydrogen to Hydrogen Peroxide. *Catal. Lett.* **2002**, *83*, 235–239. [[CrossRef](#)]
50. Choudhary, V.R.; Samanta, C. Hydrogen peroxide formation in the interaction of oxygen with boron-containing Pd catalysts prereduced by hydrazine in aqueous acidic medium containing bromide anions. *Catal. Lett.* **2005**, *99*, 79–81. [[CrossRef](#)]
51. Choudhary, V.R.; Samanta, C.; Gaikwad, A.G. Drastic increase of selectivity for H_2O_2 formation in direct oxidation of H_2 to H_2O_2 over supported Pd catalysts due to their bromination. *Chem. Commun.* **2004**, 2054–2055. [[CrossRef](#)]
52. Choudhary, V.R.; Samanta, C.; Jana, P. A novel route for in-situ H_2O_2 generation from selective reduction of O_2 by hydrazine using heterogeneous Pd catalyst in an aqueous medium. *Chem. Commun.* **2005**, 5399–5401. [[CrossRef](#)]
53. Choudhary, V.R.; Sansare, S.D.; Gaikwad, A.G. Direct Oxidation of H_2 to H_2O_2 and Decomposition of H_2O_2 Over Oxidized and Reduced Pd-Containing Zeolite Catalysts in Acidic Medium. *Catal. Lett.* **2002**, *84*, 81–87. [[CrossRef](#)]
54. Edwards, J.K.; Hutchings, G.J. Palladium and Gold–Palladium Catalysts for the Direct Synthesis of Hydrogen Peroxide. *Angew. Chem. Int. Ed.* **2008**, *47*, 9192–9198. [[CrossRef](#)]
55. Edwards, J.K.; Solsona, B.; Landon, P.; Carley, A.F.; Herzing, A.; Watanabe, M.; Kiely, C.J.; Hutchings, G.J. Direct synthesis of hydrogen peroxide from H_2 and O_2 using Au-Pd/Fe₂O₃ catalysts. *J. Mater. Chem.* **2005**, *15*, 4595–4600. [[CrossRef](#)]
56. Edwards, J.K.; Solsona, B.E.; Landon, P.; Carley, A.F.; Herzing, A.; Kiely, C.J.; Hutchings, G.J. Direct synthesis of hydrogen peroxide from H_2 and O_2 using TiO₂-supported Au-Pd catalysts. *J. Catal.* **2005**, *236*, 69–79. [[CrossRef](#)]
57. Chen, J.; Eberlein, L.; Langford, C.H. Pathways of phenol and benzene photooxidation using TiO₂ supported on a zeolite. *J. Photochem. Photobiol. A* **2002**, *148*, 183–189. [[CrossRef](#)]
58. Ahmed, S.N.; Haider, W. Heterogeneous photocatalysis and its potential applications in water and wastewater treatment: A review. *Nanotechnology* **2018**, *29*, 342001. [[CrossRef](#)]
59. Radhika, N.P.; Selvin, R.; Kakkar, R.; Umar, A. Recent advances in nano-photocatalysts for organic synthesis. *Arab. J. Chem.* **2016**. [[CrossRef](#)]
60. Kaynan, N.; Berke, B.A.; Hazut, O.; Yerushalmi, R. Sustainable photocatalytic production of hydrogen peroxide from water and molecular oxygen. *J. Mater. Chem. A* **2014**, *2*, 13822–13826. [[CrossRef](#)]
61. Carraway, E.R.; Hoffman, A.J.; Hoffmann, M.R. Photocatalytic Oxidation of Organic Acids on Quantum-Sized Semiconductor Colloids. *Environ. Sci. Technol.* **1994**, *28*, 786–793. [[CrossRef](#)]
62. Kormann, C.; Bahnemann, D.W.; Hoffmann, M.R. Photocatalytic production of hydrogen peroxides and organic peroxides in aqueous suspensions of titanium dioxide, zinc oxide, and desert sand. *Environ. Sci. Technol.* **1988**, *22*, 798–806. [[CrossRef](#)]
63. Teranishi, M.; Naya, S.I.; Tada, H. In situ liquid phase synthesis of hydrogen peroxide from molecular oxygen using gold nanoparticle-loaded titanium(IV) dioxide photocatalyst. *J. Am. Chem. Soc.* **2010**, *132*, 7850–7851. [[CrossRef](#)]
64. Zhuang, H.; Yang, L.; Xu, J.; Li, F.; Zhang, Z.; Lin, H.; Long, J.; Wang, X. Robust Photocatalytic H_2O_2 Production by Octahedral Cd₃(C₃N₃S₃)₂ Coordination Polymer under Visible Light. *Sci. Rep.* **2015**, *5*, 16947. [[CrossRef](#)]
65. Shao, D.; Zhang, L.; Sun, S.; Wang, W. Oxygen Reduction Reaction for Generating H_2O_2 through a Piezo-Catalytic Process over Bismuth Oxychloride. *ChemSusChem* **2018**, *11*, 527–531. [[CrossRef](#)]
66. Su, Y.; Zhang, L.; Wang, W.; Shao, D. Internal Electric Field Assisted Photocatalytic Generation of Hydrogen Peroxide over BiOCl with HCOOH. *ACS Sustain. Chem. Eng.* **2018**, *6*, 8704–8710. [[CrossRef](#)]

67. Isaka, Y.; Kato, S.; Hong, D.; Suenobu, T.; Yamada, Y.; Fukuzumi, S. Bottom-up and top-down methods to improve catalytic reactivity for photocatalytic production of hydrogen peroxide using a Ru-complex and water oxidation catalysts. *J. Mater. Chem. A* **2015**, *3*, 12404–12412. [[CrossRef](#)]
68. Isaka, Y.; Oyama, K.; Yamada, Y.; Suenobu, T.; Fukuzumi, S. Photocatalytic production of hydrogen peroxide from water and dioxygen using cyano-bridged polynuclear transition metal complexes as water oxidation catalysts. *Catal. Sci. Technol.* **2016**, *6*, 681–684. [[CrossRef](#)]
69. Isaka, Y.; Yamada, Y.; Suenobu, T.; Nakagawa, T.; Fukuzumi, S. Production of hydrogen peroxide by combination of semiconductor-photocatalysed oxidation of water and photocatalytic two-electron reduction of dioxygen. *RSC Adv.* **2016**, *6*, 42041–42044. [[CrossRef](#)]
70. Mase, K.; Yoneda, M.; Yamada, Y.; Fukuzumi, S. Efficient Photocatalytic Production of Hydrogen Peroxide from Water and Dioxygen with Bismuth Vanadate and a Cobalt(II) Chlorin Complex. *ACS Energy Lett.* **2016**, *1*, 913–919. [[CrossRef](#)]
71. Thakur, S.; Kshetri, T.; Kim, N.H.; Lee, J.H. Sunlight-driven sustainable production of hydrogen peroxide using a CdS–graphene hybrid photocatalyst. *J. Catal.* **2017**, *345*, 78–86. [[CrossRef](#)]
72. Charanpahari, A.; Gupta, N.; Devthade, V.; Ghugal, S.; Bhatt, J. Ecofriendly Nanomaterials for Sustainable Photocatalytic Decontamination of Organics and Bacteria. In *Handbook of Ecomaterials*; Martínez, L.M.T., Kharissova, O.V., Kharisov, B.I., Eds.; Springer International Publishing: Cham, Switzerland, 2018; pp. 1–29.
73. Chiranjeevi, T.; Pragma, R.; Gupta, S.; Gokak, D.T.; Bhargava, S. Minimization of Waste Spent Catalyst in Refineries. *Procedia Environ. Sci.* **2016**, *35*, 610–617. [[CrossRef](#)]
74. Monai, M.; Melchionna, M.; Fornasiero, P. Chapter One—From metal to metal-free catalysts: Routes to sustainable chemistry. In *Advances in Catalysis*; Song, C., Ed.; Academic Press: Cambridge, MA, USA, 2018; Volume 63, pp. 1–73.
75. Gautam, R.K.; Chattopadhyaya, M.C. Chapter 9—Magnetic Nanophotocatalysts for Wastewater Remediation. In *Nanomaterials for Wastewater Remediation*; Gautam, R.K., Chattopadhyaya, M.C., Eds.; Butterworth-Heinemann: Boston, MA, USA, 2016; pp. 189–238.
76. Shiraishi, Y.; Kanazawa, S.; Sugano, Y.; Tsukamoto, D.; Sakamoto, H.; Ichikawa, S.; Hirai, T. Highly selective production of hydrogen peroxide on graphitic carbon nitride (g-C₃N₄) photocatalyst activated by visible light. *ACS Catal.* **2014**, *4*, 774–780. [[CrossRef](#)]
77. Kofuji, Y.; Ohkita, S.; Shiraishi, Y.; Sakamoto, H.; Tanaka, S.; Ichikawa, S.; Hirai, T. Graphitic Carbon Nitride Doped with Biphenyl Diimide: Efficient Photocatalyst for Hydrogen Peroxide Production from Water and Molecular Oxygen by Sunlight. *ACS Catal.* **2016**, *6*, 7021–7029. [[CrossRef](#)]
78. Kofuji, Y.; Ohkita, S.; Shiraishi, Y.; Sakamoto, H.; Ichikawa, S.; Tanaka, S.; Hirai, T. Mellitic Triimide-Doped Carbon Nitride as Sunlight-Driven Photocatalysts for Hydrogen Peroxide Production. *ACS Sustain. Chem. Eng.* **2017**, *5*, 6478–6485. [[CrossRef](#)]
79. Ong, W.-J.; Tan, L.-L.; Ng, Y.H.; Yong, S.-T.; Chai, S.-P. Graphitic Carbon Nitride (g-C₃N₄)-Based Photocatalysts for Artificial Photosynthesis and Environmental Remediation: Are We a Step Closer To Achieving Sustainability? *Chem. Rev.* **2016**, *116*, 7159–7329. [[CrossRef](#)] [[PubMed](#)]
80. Patnaik, S.; Martha, S.; Acharya, S.; Parida, K.M. An overview of the modification of g-C₃N₄ with high carbon containing materials for photocatalytic applications. *Inorg. Chem. Front.* **2016**, *3*, 336–347. [[CrossRef](#)]
81. Zhao, Z.; Sun, Y.; Dong, F. Graphitic carbon nitride based nanocomposites: A review. *Nanoscale* **2015**, *7*, 15–37. [[CrossRef](#)] [[PubMed](#)]
82. Zhang, G.; Lan, Z.A.; Wang, X. Surface engineering of graphitic carbon nitride polymers with cocatalysts for photocatalytic overall water splitting. *Chem. Sci.* **2017**, *8*, 5261–5274. [[CrossRef](#)]
83. Mamba, G.; Mishra, A.K. Graphitic carbon nitride (g-C₃N₄) nanocomposites: A new and exciting generation of visible light driven photocatalysts for environmental pollution remediation. *Appl. Catal. B Environ.* **2016**, *198*, 347–377. [[CrossRef](#)]
84. Lima, M.J.; Silva, A.M.T.; Silva, C.G.; Faria, J.L. Graphitic carbon nitride modified by thermal, chemical and mechanical processes as metal-free photocatalyst for the selective synthesis of benzaldehyde from benzyl alcohol. *J. Catal.* **2017**, *353*, 44–53. [[CrossRef](#)]
85. Wang, Y.; Wang, X.; Antonietti, M. Polymeric Graphitic Carbon Nitride as a Heterogeneous Organocatalyst: From Photochemistry to Multipurpose Catalysis to Sustainable Chemistry. *Angew. Chem. Int. Ed.* **2012**, *51*, 68–89. [[CrossRef](#)]

86. Domcke, W.; Ehrmaier, J.; Sobolewski, A.L. Solar Energy Harvesting with Carbon Nitrides and N-Heterocyclic Frameworks: Do We Understand the Mechanism? *ChemPhotoChem* **2019**, *3*, 10–23. [[CrossRef](#)]
87. Corp, K.L.; Schlenker, C.W. Ultrafast Spectroscopy Reveals Electron-Transfer Cascade That Improves Hydrogen Evolution with Carbon Nitride Photocatalysts. *J. Am. Chem. Soc.* **2017**, *139*, 7904–7912. [[CrossRef](#)]
88. Haider, Z.; Cho, H.-I.; Moon, G.-H.; Kim, H.-I. Minireview: Selective production of hydrogen peroxide as a clean oxidant over structurally tailored carbon nitride photocatalysts. *Catal. Today* **2018**, *335*, 55–64. [[CrossRef](#)]
89. Goto, H.; Hanada, Y.; Ohno, T.; Matsumura, M. Quantitative analysis of superoxide ion and hydrogen peroxide produced from molecular oxygen on photoirradiated TiO₂ particles. *J. Catal.* **2004**, *225*, 223–229. [[CrossRef](#)]
90. Maurino, V.; Minero, C.; Mariella, G.; Pelizzetti, E. Sustained production of H₂O₂ on irradiated TiO₂—Fluoride systems. *Chem. Commun.* **2005**, 2627–2629. [[CrossRef](#)] [[PubMed](#)]
91. Hirakawa, T.; Nosaka, Y. Selective Production of Superoxide Ions and Hydrogen Peroxide over Nitrogen- and Sulfur-Doped TiO₂ Photocatalysts with Visible Light in Aqueous Suspension Systems. *J. Phys. Chem. C* **2008**, *112*, 15818–15823. [[CrossRef](#)]
92. Tsukamoto, D.; Shiro, A.; Shiraishi, Y.; Sugano, Y.; Ichikawa, S.; Tanaka, S.; Hirai, T. Photocatalytic H₂O₂ Production from Ethanol/O₂ System Using TiO₂ Loaded with Au–Ag Bimetallic Alloy Nanoparticles. *ACS Catal.* **2012**, *2*, 599–603. [[CrossRef](#)]
93. Cai, R.; Kubota, Y.; Fujishima, A. Effect of copper ions on the formation of hydrogen peroxide from photocatalytic titanium dioxide particles. *J. Catal.* **2003**, *219*, 214–218. [[CrossRef](#)]
94. Shiraishi, Y.; Kofuji, Y.; Sakamoto, H.; Tanaka, S.; Ichikawa, S.; Hirai, T. Effects of Surface Defects on Photocatalytic H₂O₂ Production by Mesoporous Graphitic Carbon Nitride under Visible Light Irradiation. *ACS Catal.* **2015**, *5*, 3058–3066. [[CrossRef](#)]
95. Zhang, H.; Guo, L.-H.; Zhao, L.; Wan, B.; Yang, Y. Switching Oxygen Reduction Pathway by Exfoliating Graphitic Carbon Nitride for Enhanced Photocatalytic Phenol Degradation. *J. Phys. Chem. Lett.* **2015**, *6*, 958–963. [[CrossRef](#)]
96. Yang, L.; Dong, G.; Jacobs, D.L.; Wang, Y.; Zang, L.; Wang, C. Two-channel photocatalytic production of H₂O₂ over g-C₃N₄ nanosheets modified with perylene imides. *J. Catal.* **2017**, *352*, 274–281. [[CrossRef](#)]
97. Perry, S.C.; Pangothra, D.; Vieira, L.; Csepei, L.-I.; Sieber, V.; Wang, L.; Ponce de León, C.; Walsh, F.C. Electrochemical synthesis of hydrogen peroxide from water and oxygen. *Nat. Rev. Chem.* **2019**, *3*, 442–458. [[CrossRef](#)]
98. Cui, Y.; Ding, Z.; Liu, P.; Antonietti, M.; Fu, X.; Wang, X. Metal-free activation of H₂O₂ by g-C₃N₄ under visible light irradiation for the degradation of organic pollutants. *Phys. Chem. Chem. Phys.* **2012**, *14*, 1455–1462. [[CrossRef](#)]
99. Chen, J.; Wagner, P.; Tong, L.; Wallace, G.G.; Officer, D.L.; Swiegers, G.F. A Porphyrin-Doped Polymer Catalyzes Selective, Light-Assisted Water Oxidation in Seawater. *Angew. Chem. Int. Ed.* **2012**, *51*, 1907–1910. [[CrossRef](#)] [[PubMed](#)]
100. Koppenol, W.H. Oxygen Activation by Cytochrome P450: A Thermodynamic Analysis. *J. Am. Chem. Soc.* **2007**, *129*, 9686–9690. [[CrossRef](#)] [[PubMed](#)]
101. David, A.A.; Robert, E.H.; Willem, H.K.; Sergei, V.L.; Merényi, G.; Neta, P.; Ruscic, B.; David, M.S.; Steenken, S.; Wardman, P. Standard electrode potentials involving radicals in aqueous solution: Inorganic radicals (IUPAC Technical Report). *Pure Appl. Chem.* **2015**, *87*, 1139.
102. Ghaly, M.Y.; Härtel, G.; Mayer, R.; Haseneder, R. Photochemical oxidation of p-chlorophenol by UV/H₂O₂ and photo-Fenton process. A comparative study. *Waste Manag.* **2001**, *21*, 41–47. [[CrossRef](#)]
103. Macías-Sánchez, J.; Hinojosa-Reyes, L.; Guzmán-Mar, J.L.; Peralta-Hernández, J.M.; Hernández-Ramírez, A. Performance of the photo-Fenton process in the degradation of a model azo dye mixture. *Photochem. Photobiol. Sci.* **2011**, *10*, 332–337. [[CrossRef](#)]
104. Pérez-Moya, M.; Graells, M.; Castells, G.; Amigó, J.; Ortega, E.; Buhigas, G.; Pérez, L.M.; Mansilla, H.D. Characterization of the degradation performance of the sulfamethazine antibiotic by photo-Fenton process. *Water Res.* **2010**, *44*, 2533–2540. [[CrossRef](#)]
105. Li, S.; Dong, G.; Hailili, R.; Yang, L.; Li, Y.; Wang, F.; Zeng, Y.; Wang, C. Effective photocatalytic H₂O₂ production under visible light irradiation at g-C₃N₄ modulated by carbon vacancies. *Appl. Catal. B Environ.* **2016**, *190*, 26–35. [[CrossRef](#)]

106. Zhao, S.; Guo, T.; Li, X.; Xu, T.; Yang, B.; Zhao, X. Carbon nanotubes covalent combined with graphitic carbon nitride for photocatalytic hydrogen peroxide production under visible light. *Appl. Catal. B Environ.* **2018**, *224*, 725–732. [[CrossRef](#)]
107. Shiraishi, Y.; Kanazawa, S.; Kofuji, Y.; Sakamoto, H.; Ichikawa, S.; Tanaka, S.; Hirai, T. Sunlight-driven hydrogen peroxide production from water and molecular oxygen by metal-free photocatalysts. *Angew. Chem. Int. Ed.* **2014**, *53*, 13454–13459. [[CrossRef](#)]
108. Kim, H.-I.; Choi, Y.; Hu, S.; Choi, W.; Kim, J.-H. Photocatalytic hydrogen peroxide production by anthraquinone-augmented polymeric carbon nitride. *Appl. Catal. B Environ.* **2018**, *229*, 121–129. [[CrossRef](#)]
109. Shi, L.; Yang, L.; Zhou, W.; Liu, Y.; Yin, L.; Hai, X.; Song, H.; Ye, J. Photoassisted Construction of Holey Defective g-C₃N₄ Photocatalysts for Efficient Visible-Light-Driven H₂O₂ Production. *Small* **2018**, *14*, 1703142. [[CrossRef](#)] [[PubMed](#)]
110. Zhu, Z.; Pan, H.; Murugananthan, M.; Gong, J.; Zhang, Y. Visible light-driven photocatalytically active g-C₃N₄ material for enhanced generation of H₂O₂. *Appl. Catal. B Environ.* **2018**, *232*, 19–25. [[CrossRef](#)]
111. Qu, X.; Hu, S.; Li, P.; Li, Z.; Wang, H.; Ma, H.; Li, W. The effect of embedding N vacancies into g-C₃N₄ on the photocatalytic H₂O₂ production ability via H₂ plasma treatment. *Diam. Relat. Mater.* **2018**, *86*, 159–166. [[CrossRef](#)]
112. Wang, R.; Zhang, X.; Li, F.; Cao, D.; Pu, M.; Han, D.; Yang, J.; Xiang, X. Energy-level dependent H₂O₂ production on metal-free, carbon-content tunable carbon nitride photocatalysts. *J. Energy Chem.* **2018**, *27*, 343–350. [[CrossRef](#)]
113. Moon, G.-H.; Kim, W.; Bokare, A.D.; Sung, N.-E.; Choi, W. Solar production of H₂O₂ on reduced graphene oxide–TiO₂ hybrid photocatalysts consisting of earth-abundant elements only. *Energy Environ. Sci.* **2014**, *7*, 4023–4028. [[CrossRef](#)]
114. Kim, H.; Gim, S.; Jeon, T.H.; Kim, H.; Choi, W. Distorted Carbon Nitride Structure with Substituted Benzene Moieties for Enhanced Visible Light Photocatalytic Activities. *ACS Appl. Mater. Interfaces* **2017**, *9*, 40360–40368. [[CrossRef](#)]
115. Dong, S.; Liu, C.; Chen, Y. Boosting exciton dissociation and molecular oxygen activation by in-plane grafting nitrogen-doped carbon nanosheets to graphitic carbon nitride for enhanced photocatalytic performance. *J. Colloid Interface Sci.* **2019**, *553*, 59–70. [[CrossRef](#)]
116. Wang, H.; Guan, Y.; Hu, S.; Pei, Y.; Ma, W.; Fan, Z. Hydrothermal Synthesis of Band Gap-Tunable Oxygen-Doped g-C₃N₄ with Outstanding “two-Channel” Photocatalytic H₂O₂ Production Ability Assisted by Dissolution-Precipitation Process. *Nano* **2019**, *14*, 1950023. [[CrossRef](#)]
117. Bai, J.; Sun, Y.; Li, M.; Yang, L.; Li, J. The effect of phosphate modification on the photocatalytic H₂O₂ production ability of g-C₃N₄ catalyst prepared via acid-hydrothermal post-treatment. *Diam. Relat. Mater.* **2018**, *87*, 1–9. [[CrossRef](#)]
118. Zang, L. Interfacial Donor–Acceptor Engineering of Nanofiber Materials To Achieve Photoconductivity and Applications. *Acc. Chem. Res.* **2015**, *48*, 2705–2714. [[CrossRef](#)]
119. Kofuji, Y.; Isobe, Y.; Shiraishi, Y.; Sakamoto, H.; Tanaka, S.; Ichikawa, S.; Hirai, T. Carbon Nitride-Aromatic Diimide-Graphene Nanohybrids: Metal-Free Photocatalysts for Solar-to-Hydrogen Peroxide Energy Conversion with 0.2% Efficiency. *J. Am. Chem. Soc.* **2016**, *138*, 10019–10025. [[CrossRef](#)]
120. Yang, Y.; Zhang, C.; Huang, D.; Zeng, G.; Huang, J.; Lai, C.; Zhou, C.; Wang, W.; Guo, H.; Xue, W.; et al. Boron nitride quantum dots decorated ultrathin porous g-C₃N₄: Intensified exciton dissociation and charge transfer for promoting visible-light-driven molecular oxygen activation. *Appl. Catal. B Environ.* **2019**, *245*, 87–99. [[CrossRef](#)]
121. He, Z.; Kim, C.; Lin, L.; Jeon, T.H.; Lin, S.; Wang, X.; Choi, W. Formation of heterostructures via direct growth CN on h-BN porous nanosheets for metal-free photocatalysis. *Nano Energy* **2017**, *42*, 58–68. [[CrossRef](#)]
122. Kofuji, Y.; Isobe, Y.; Shiraishi, Y.; Sakamoto, H.; Ichikawa, S.; Tanaka, S.; Hirai, T. Hydrogen Peroxide Production on a Carbon Nitride–Boron Nitride-Reduced Graphene Oxide Hybrid Photocatalyst under Visible Light. *ChemCatChem* **2018**, *10*, 2070–2077. [[CrossRef](#)]
123. Wang, H.; Zhang, L.; Chen, Z.; Hu, J.; Li, S.; Wang, Z.; Liu, J.; Wang, X. Semiconductor heterojunction photocatalysts: Design, construction, and photocatalytic performances. *Chem. Soc. Rev.* **2014**, *43*, 5234–5244. [[CrossRef](#)] [[PubMed](#)]

124. Zheng, Y.; Yu, Z.; Ou, H.; Asiri, A.M.; Chen, Y.; Wang, X. Black Phosphorus and Polymeric Carbon Nitride Heterostructure for Photoinduced Molecular Oxygen Activation. *Adv. Funct. Mater.* **2018**, *28*, 1705407. [[CrossRef](#)]
125. Li, R.; Li, C. Chapter One—Photocatalytic Water Splitting on Semiconductor-Based Photocatalysts. In *Advances in Catalysis*; Song, C., Ed.; Academic Press: Cambridge, MA, USA, 2017; Volume 60, pp. 1–57.
126. Chen, Y.-C.; Smirniotis, P. Enhancement of Photocatalytic Degradation of Phenol and Chlorophenols by Ultrasound. *Ind. Eng. Chem. Res.* **2002**, *41*, 5958–5965. [[CrossRef](#)]
127. Qin, T.; You, Z.; Wang, H.; Shen, Q.; Zhang, F.; Yang, H. Preparation and photocatalytic behavior of carbon-nanodots/graphitic carbon nitride composite photocatalyst. *J. Electrochem. Soc.* **2017**, *164*, H211–H214. [[CrossRef](#)]
128. Desipio, M.M.; Thorpe, R.; Saha, D. Photocatalytic Decomposition of Paraquat Under Visible Light by Carbon Nitride and Hydrogen Peroxide. *Optik* **2018**, *172*, 1047–1056. [[CrossRef](#)]
129. Wang, X.; Li, D.; Nan, Z. Effect of N content in g-C₃N₄ as metal-free catalyst on H₂O₂ decomposition for MB degradation. *Sep. Purif. Technol.* **2019**, *224*, 152–162. [[CrossRef](#)]
130. Dinesh, G.K.; Chakma, S. Mechanistic investigation in degradation mechanism of 5-fluorouracil using graphitic carbon nitride. *Ultrason. Sonochem.* **2019**, *50*, 311–321. [[CrossRef](#)] [[PubMed](#)]
131. Teng, Z.; Yang, N.; Lv, H.; Wang, S.; Hu, M.; Wang, C.; Wang, D.; Wang, G. Edge-Functionalized g-C₃N₄ Nanosheets as a Highly Efficient Metal-free Photocatalyst for Safe Drinking Water. *Chem* **2019**, *5*, 664–680. [[CrossRef](#)]
132. Saha, D.; Desipio, M.M.; Hoinkis, T.J.; Smeltz, E.J.; Thorpe, R.; Hensley, D.K.; Fischer-Drowos, S.G.; Chen, J. Influence of hydrogen peroxide in enhancing photocatalytic activity of carbon nitride under visible light: An insight into reaction intermediates. *J. Environ. Chem. Eng.* **2018**, *6*, 4927–4936. [[CrossRef](#)]
133. Chen, Q.L.; Liu, Y.L.; Tong, L.G. Enhanced visible light photocatalytic activity of g-C₃N₄ assisted by hydrogen peroxide. *Mater. Res. Express* **2018**, *5*, 046203. [[CrossRef](#)]
134. Wu, Q.; He, Y.; Zhang, H.; Feng, Z.; Wu, Y.; Wu, T. Photocatalytic selective oxidation of biomass-derived 5-hydroxymethylfurfural to 2,5-diformylfuran on metal-free g-C₃N₄ under visible light irradiation. *Mol. Catal.* **2017**, *436*, 10–18. [[CrossRef](#)]
135. Jiang, L.; Yuan, X.; Zeng, G.; Wu, Z.; Liang, J.; Chen, X.; Leng, L.; Wang, H.; Wang, H. Metal-free efficient photocatalyst for stable visible-light photocatalytic degradation of refractory pollutant. *Appl. Catal. B Environ.* **2018**, *221*, 715–725. [[CrossRef](#)]
136. Wang, H.; Su, Y.; Zhao, H.; Yu, H.; Chen, S.; Zhang, Y.; Quan, X. Photocatalytic oxidation of aqueous ammonia using atomic single layer graphitic-C₃N₄. *Environ. Sci. Technol.* **2014**, *48*, 11984–11990. [[CrossRef](#)]
137. Zhang, Q.; Chen, P.; Tan, C.; Chen, T.; Zhuo, M.; Xie, Z.; Wang, F.; Liu, H.; Cai, Z.; Liu, G.; et al. A photocatalytic degradation strategy of PPCPs by a heptazine-based CN organic polymer (OCN) under visible light. *Environ. Sci. Nano* **2018**, *5*, 2325–2336. [[CrossRef](#)]
138. Wang, H.; Guo, H.; Zhang, N.; Chen, Z.; Hu, B.; Wang, X. Enhanced Photoreduction of U(VI) on C₃N₄ by Cr(VI) and Bisphenol A: ESR, XPS, and EXAFS Investigation. *Environ. Sci. Technol.* **2019**, *53*, 6454–6461. [[CrossRef](#)]
139. Wang, Z.; Murugananthan, M.; Zhang, Y. Graphitic carbon nitride based photocatalysis for redox conversion of arsenic(III) and chromium(VI) in acid aqueous solution. *Appl. Catal. B Environ.* **2019**, *248*, 349–356. [[CrossRef](#)]
140. Wang, H.; Li, Q.; Zhang, S.; Chen, Z.; Wang, W.; Zhao, G.; Zhuang, L.; Hu, B.; Wang, X. Visible-light-driven N₂-g-C₃N₄ as a highly stable and efficient photocatalyst for bisphenol A and Cr(VI) removal in binary systems. *Catal. Today* **2019**, *335*, 110–116. [[CrossRef](#)]
141. Chen, J.; Xu, X.; Li, T.; Pandiselvi, K.; Wang, J. Toward High Performance 2D/2D Hybrid Photocatalyst by Electrostatic Assembly of Rationally Modified Carbon Nitride on Reduced Graphene Oxide. *Sci. Rep.* **2016**, *6*, 37318. [[CrossRef](#)]
142. Svoboda, L.; Praus, P.; Lima, M.J.; Sampaio, M.J.; Matýšek, D.; Ritz, M.; Dvorský, R.; Faria, J.L.; Silva, C.G. Graphitic carbon nitride nanosheets as highly efficient photocatalysts for phenol degradation under high-power visible LED irradiation. *Mater. Res. Bull.* **2018**, *100*, 322–332. [[CrossRef](#)]
143. Yazici, E.; Deveci, H. Factors Affecting Decomposition of Hydrogen Peroxide. In Proceedings of the XIIth International Mineral Processing Symposium, Cappadocia-Nevşehir, Turkey, 6 October 2010; pp. 609–616.

144. Cheng, F.; Wang, H.; Dong, X. The amphoteric properties of g-C₃N₄ nanosheets and fabrication of their relevant heterostructure photocatalysts by an electrostatic re-assembly route. *Chem. Commun.* **2015**, *51*, 7176–7179. [[CrossRef](#)] [[PubMed](#)]
145. Bicheng, Z.; Xia, P.; Ho, W.; Yu, J. Isoelectric point and adsorption activity of porous g-C₃N₄. *Appl. Surf. Sci.* **2015**, *344*, 188–195.
146. Torres-Pinto, A.; Sampaio, M.J.; Silva, C.G.; Faria, J.L.; Silva, A.M.T. Metal-free carbon nitride photocatalysis with in-situ hydrogen peroxide generation for the degradation of aromatic compounds. *Appl. Catal. B Environ.* **2019**, *252*, 128–137. [[CrossRef](#)]
147. Hu, J.-Y.; Tian, K.; Jiang, H. Improvement of phenol photodegradation efficiency by a combined g-C₃N₄/Fe(III)/persulfate system. *Chemosphere* **2016**, *148*, 34–40. [[CrossRef](#)]
148. Yuan, X.; Xie, R.; Zhang, Q.; Sun, L.; Long, X.; Xia, D. Oxygen functionalized graphitic carbon nitride as an efficient metal-free ozonation catalyst for atrazine removal: Performance and mechanism. *Sep. Purif. Technol.* **2019**, *211*, 823–831. [[CrossRef](#)]
149. Li, X.; Pi, Y.; Wu, L.; Xia, Q.; Wu, J.; Li, Z.; Xiao, J. Facilitation of the visible light-induced Fenton-like excitation of H₂O₂ via heterojunction of g-C₃N₄/NH₂-Iron terephthalate metal-organic framework for MB degradation. *Appl. Catal. B Environ.* **2017**, *202*, 653–663. [[CrossRef](#)]
150. Ren, S.; Chen, C.; Zhou, Y.; Dong, Q.; Ding, H. The α-Fe₂O₃/g-C₃N₄ composite as an efficient heterogeneous catalyst with combined Fenton and photocatalytic effects. *Res. Chem. Intermediat.* **2017**, *43*, 3307–3323. [[CrossRef](#)]
151. Desipio, M.M.; Van Bramer, S.E.; Thorpe, R.; Saha, D. Photocatalytic and photo-fenton activity of iron oxide-doped carbon nitride in 3D printed and LED driven photon concentrator. *J. Hazard. Mater.* **2019**, *376*, 178–187. [[CrossRef](#)] [[PubMed](#)]
152. Ding, Q.; Lam, F.L.Y.; Hu, X. Complete degradation of ciprofloxacin over g-C₃N₄-iron oxide composite via heterogeneous dark Fenton reaction. *J. Environ. Manag.* **2019**, *244*, 23–32. [[CrossRef](#)] [[PubMed](#)]
153. Pedrosa, M.; Sampaio, M.J.; Horvat, T.; Nunes, O.C.; Dražić, G.; Rodrigues, A.E.; Figueiredo, J.L.; Silva, C.G.; Silva, A.M.T.; Faria, J.L. Visible-light-induced self-cleaning functional fabrics using graphene oxide/carbon nitride materials. *Appl. Surf. Sci.* **2019**, *497*, 143757. [[CrossRef](#)]
154. Moreira, N.F.F.; Sampaio, M.J.; Ribeiro, A.R.; Silva, C.G.; Faria, J.L.; Silva, A.M.T. Metal-free g-C₃N₄ photocatalysis of organic micropollutants in urban wastewater under visible light. *Appl. Catal. B Environ.* **2019**, *248*, 184–192. [[CrossRef](#)]
155. Wang, Y.; Li, H.; Yao, J.; Wang, X.; Antonietti, M. Synthesis of boron doped polymeric carbon nitride solids and their use as metal-free catalysts for aliphatic C-H bond oxidation. *Chem. Sci.* **2011**, *2*, 446–450. [[CrossRef](#)]
156. Min, B.H.; Ansari, M.B.; Mo, Y.H.; Park, S.E. Mesoporous carbon nitride synthesized by nanocasting with urea/formaldehyde and metal-free catalytic oxidation of cyclic olefins. *Catal. Today* **2013**, *204*, 156–163. [[CrossRef](#)]
157. Lopes, J.C.; Sampaio, M.J.; Fernandes, R.A.; Lima, M.J.; Faria, J.L.; Silva, C.G. Outstanding response of carbon nitride photocatalysts for selective synthesis of aldehydes under UV-LED irradiation. *Catal. Today* **2019**. [[CrossRef](#)]
158. Zhang, J.J.; Ge, J.M.; Wang, H.H.; Wei, X.; Li, X.H.; Chen, J.S. Activating Oxygen Molecules over Carbonyl-Modified Graphitic Carbon Nitride: Merging Supramolecular Oxidation with Photocatalysis in a Metal-Free Catalyst for Oxidative Coupling of Amines into Imines. *ChemCatChem* **2016**, *8*, 3441–3445. [[CrossRef](#)]

